Journal of Photochemistry & Photobiology, B: Biology 254 (2024) 112903

Contents lists available at ScienceDirect

Journal of Photochemistry & Photobiology, B: Biology

journal homepage: www.elsevier.com/locate/jphotobiol

Comparative analysis of whole cell-derived vesicular delivery systems for photodynamic therapy of extrahepatic cholangiocarcinoma

Mingjuan Li [a,b], Esmeralda D.C. Bosman [b], Olivia M. Smith [c,d], Nicole Lintern [c,d], Daniel J. de Klerk [a], Hong Sun [e,f], Shuqun Cheng [g], Weiwei Pan [h], Gert Storm [b], Yazan S. Khaled [c,d,**], Michal Heger [a,b,i,*], on behalf of the Photodynamic Therapy Study Group

[a] Jiaxing Key Laboratory for Photonanomedicine and Experimental Therapeutics, Department of Pharmaceutics, College of Medicine, Jiaxing University, 314001 Jiaxing, Zhejiang, PR China
[b] Department of Pharmaceutics, Utrecht Institute for Pharmaceutical Sciences, Utrecht University, 3584 CS Utrecht, the Netherlands
[c] Leeds Institute of Medical Research, St. James's University Hospital, Leeds LS9 7TF, United Kingdom
[d] The University of Leeds, School of Medicine, Leeds LS2 9JT, United Kingdom
[e] Key Laboratory of Medical Electronics and Digital Health of Zhejiang Province, Jiaxing University, 314001 Jiaxing, Zhejiang, PR China
[f] Engineering Research Center of Intelligent Human Health Situation Awareness of Zhejiang Province, Jiaxing University, 314001 Jiaxing, Zhejiang, PR China
[g] Department of Hepatic Surgery VI, The Eastern Hepatobiliary Surgery Hospital, The Second Military Medical University, 200433 Shanghai, PR China
[h] Department of Cell Biology, College of Medicine, Jiaxing University, 314001 Jiaxing, Zhejiang, PR China
[i] Membrane Biochemistry and Biophysics, Department of Chemistry, Faculty of Science, Utrecht University, 3584 CS Utrecht, the Netherlands

ARTICLE INFO

Keywords:
Anti-cancer treatment
Biliary tumors
Reactive oxygen species
Oxidative stress
Cell death
Targeted photosensitizer delivery
Photosensitized
Vesicles
Endocytosis
Intracellular distribution

ABSTRACT

This first-in-its-class proof-of-concept study explored the use of bionanovesicles for the delivery of photosensitizer into cultured cholangiocarcinoma cells and subsequent treatment by photodynamic therapy (PDT). Two types of bionanovesicles were prepared: cellular vesicles (CVs) were fabricated by sonication-mediated nanosizing of cholangiocarcinoma (TFK-1) cells, whereas cell membrane vesicles (CMVs) were produced by TFK-1 cell and organelle membrane isolation and subsequent nanovesicularization by sonication. The bionanovesicles were loaded with zinc phthalocyanine (ZnPC). The CVs and CMVs were characterized (size, polydispersity index, zeta potential, stability, ZnPC encapsulation efficiency, spectral properties) and assayed for tumor (TFK-1) cell association and uptake (flow cytometry, confocal microscopy), intracellular ZnPC distribution (confocal microscopy), dark toxicity (MTS assay), and PDT efficacy (MTS assay). The mean ± SD diameter, polydispersity index, and zeta potential were 134 ± 1 nm, −16.1 ± 0.9, and 0.220 ± 0.013, respectively, for CVs and 172 ± 3 nm, −16.4 ± 1.1, and 0.167 ± 0.022, respectively, for CMVs. Cold storage for 1 wk and incorporation of ZnPC increased bionanovesicular diameter slightly but size remained within the recommended range for in vivo application (136–220 nm). ZnPC was incorporated into CVs and CMVs at an optimal photosensitizer:lipid molar ratio of 0.006 and 0.01, respectively. Both bionanovesicles were avidly taken up by TFK-1 cells, resulting in homogenous intracellular ZnPC dispersion. Photosensitization of TFK-1 cells did not cause dark toxicity, while illumination at 671 nm (35.3 J/cm^2) produced LC_{50} values of 1.11 μM (CVs) and 0.51 μM (CMVs) at 24 h post-PDT, which is superior to most LC_{50} values generated in tumor cells photosensitized with liposomal ZnPC. In conclusion, CVs and CMVs constitute a potent photosensitizer platform with no inherent cytotoxicity and high PDT efficacy in vitro.

* Correspondence to: M. Heger, Jiaxing Key Laboratory for Photonanomedicine and Experimental Therapeutics, Department of Pharmaceutics, College of Medicine, Jiaxing University, 314001 Jiaxing, Zhejiang, PR China.
** Correspondence to: Y.S. Khaled, Leeds Institute of Medical Research, St. James's University Hospital, Leeds LS9 7TF, United Kingdom.
E-mail addresses: limingjuan@zjxu.edu.cn (M. Li), e.d.c.bosman@uu.nl (E.D.C. Bosman), um21nml@leeds.ac.uk (N. Lintern), hongsun@zjxu.edu.cn (H. Sun), g.storm@uu.nl (G. Storm), y.khaled@leeds.ac.uk (Y.S. Khaled), michal.heger@photonanomedicine.com (M. Heger).

https://doi.org/10.1016/j.jphotobiol.2024.112903
Received 9 January 2024; Received in revised form 26 March 2024; Accepted 1 April 2024
Available online 2 April 2024

1. Introduction

Conventional treatment modalities for cancer include chemotherapy, radiotherapy, and surgery and their implementation depends on the primary origin, stage, and metastasis state of the tumor. The treatments are associated with various complications, including morbidity, adverse systemic effects, toxicity, and multidrug resistance. Alternative and experimental approaches such as cell therapy, gene therapy, immunotherapy, and targeted therapy have yielded promising results [1–5] but also come with drawbacks that include high costs, toxicity, low efficacy in non-indicated cancer types, and the risk of failure in advanced clinical trials. It is therefore important to keep developing novel interventions that are non-to-minimally invasive, tumor-specific, non-toxic, and affordable for patients regardless of economic class. These experimental therapies could be deployed in a substitutive or complementary manner to currently used modalities.

Photodynamic therapy (PDT, Fig. 1) is such a treatment strategy that is explored for numerous types of solid tumors that arise in internal organs and organ structures [6], including non-resectable extrahepatic cholangiocarcinoma [7–12]. Non-resectable extrahepatic cholangiocarcinoma is currently incurable and responds poorly to chemotherapy [13]. PDT has shown promise for this malignancy [14–18] but widespread clinical implementation has stalled in part due to the following reasons. Clinical caveats of PDT with approved PSs entail long-term skin photosensitivity that could lead to (severe) photoallergic reactions [12] and corollary ethical concerns over indoors-ridden patients who only have a few months to live [19,20]. Moreover, there are noncircumventable photophysical restrictions that dictate outcome. Insufficient optical penetration of laser light precludes efficient photokilling across the entire tumor volume, especially in bulkier tumors [21]. Consequently, distally located tumor cells are sublethally afflicted by PDT [9] and in response activate survival mechanisms to remedy the hyperoxidative stress and cell damage [11,21–23], which enables the tumor cells to cope and ultimately accounts for tumor regrowth [24,25]. Nonetheless, PDT has several advantages over aforementioned treatments that warrant continued research, namely (1) the doubly selective nature of the treatment [12]; (2) general lack of systemic toxicity of photosensitizers [20]; (3) no development of drug resistance by tumor cells (applies to some PSs) [26,27]; (4) abscopal removal of residually viable tumor cells and metastases as secondary treatment effect [28,29], and (5) relatively low cost [20].

Our group has instituted measures to counter these PDT-specific clinical bottlenecks through the use of third-generation [20] and fourth-generation metallated phthalocyanine-based PSs [8,10,30] that are targeted to pharmacologically relevant locations in the tumor: the tumor microenvironment [7,9,12,19], the tumor endothelium [8,10,11,30,31], and the tumor parenchyma [32]. Liposomes are used to solubilize the lipophilic phthalocyanines and to encapsulate the PS molecules so as to sterically deter PS extravasation through the cutaneous microcirculation and minimize skin photosensitization. The simplest formulation – the interstitially targeted liposomes (ITLs) – encapsulating the PS zinc phthalocyanine (ZnPC) at a 0.003 PS:lipid ratio was shown to be taken up by all relevant cell types in vitro, including tumor cells (A431 [19], SK-ChA-1 [12]), endothelial cells (HUVECs) [12], fibroblasts (NIH-3T3) [12], and macrophages (RAW 264.7) [12], despite the PEGylation. The extensive cell photosensitization yielded a 50% lethal concentration (LC_{50}) range from 0.16 μM (SK-ChA-1 cells) to 2.03 μM (fibroblasts) 24 h after PDT of cell monolayers [12]. This formulation, consisting of DPPC and DSPE-PEG at a 96:4 molar ratio, did not confer notable dark toxicity in multiple species (human and murine cell lines, zebrafish, chicken embryos, and mice) and was associated with moderate skin phototoxicity in vivo under exaggerated light conditions [12]. In mice bearing human triple negative breast cancer (MDA-MB-231) xenografts, the ZnPC-ITLs caused a 4-day (33%) delay in tumors reaching the human endpoint (tumor volume of $\geq$1800 mm^3) after a single PDT session (starting tumor volume of 100–200 mm^3, single *i.v.* bolus of 6 nmol ZnPC/animal, 24-h drug-light interval, 671-nm diode laser, cumulative radiant exposure of 200 J/cm^2) compared to untreated tumor controls. At an administered PS dose that was 2 orders of magnitude lower than used in other comparable studies [33–35], the therapeutic efficacy in breast cancer xenografts was non-inferior in terms of tumor volume reduction [12].

Although the in vivo results with the ZnPC-ITLs provided satisfactory proof-of-concept at non-optimized conditions [12], a moderate degree of skin phototoxicity and semi-synthetic make-up of PEGylated liposomes are unacceptable and clinically risk-laden, respectively. In terms of the latter, liposomes can activate the complement system [36,37] and PEGylated liposomes can trigger accelerated blood clearance [38] due to a humoral immune response against PEG (anti-PEG IgM) after the first injection [39] and hepatic and splenic clearance of PEGylated particles in subsequent exposures [38,40]. This issue should not be underestimated in the wake of the recently developed mRNA vaccines, which contain both phospholipids and PEG [41]. Liposomes may also be cleared from the circulation by cells of the reticuloendothelial system (RES), reducing the effective dosage at the target site to therapeutically moot levels [42,43]. The accumulation of liposomes in macrophages, especially at higher doses, can influence the phagocytic activity, leading to immune suppression and hampered pathogen clearance [42,44,45] as

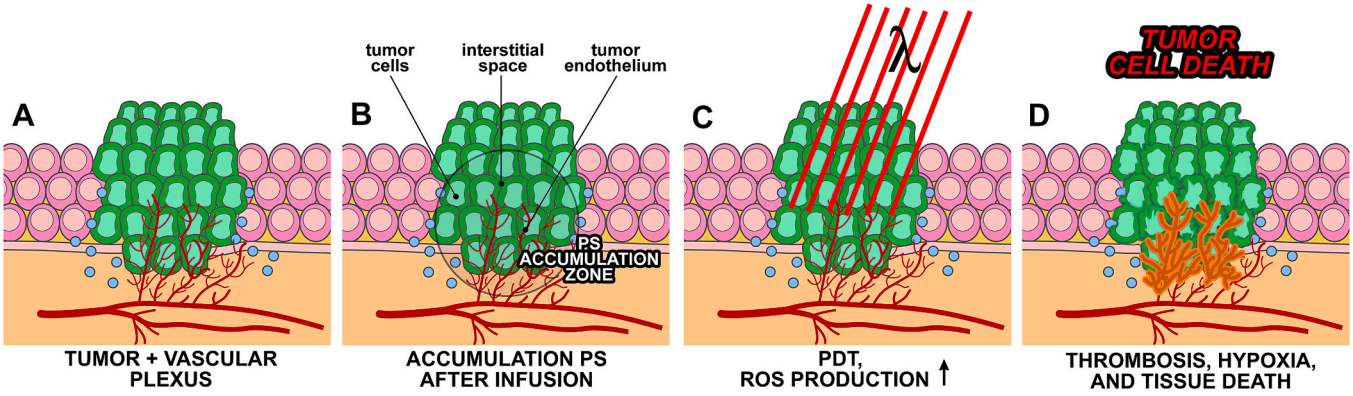

Fig. 1. Mechanistic overview of photodynamic therapy (PDT) of solid tumors, the anatomy of which is schematically depicted in (A). (B) After systemic administration of the photosensitizer (PS), the PS targets to the malignancy via the circulation and gradually accumulates in the tumor (encircled) as a result of the enhanced permeability and retention (EPR) effect. (C) Following PS accumulation in the tumor, the tumor tissue is illuminated ("λ") to activate the PS. Activated PSs produce reactive oxygen species (ROS). (D) The ROS subsequently cause oxidation of biomolecules and oxidative damage to cells in the PS-containing illuminated region, resulting in tumor cell death, thrombosis-mediated vascular shutdown and consequent hypoxia, and an anti-tumor immune response that mediates immunological cell death, altogether accounting for the removal of the tumor [20].

well as reduced anti-tumor immune responsiveness [46]. Furthermore, the liposome preparation process requires organic solvents and chemicals [47–50] that may not be biocompatible or GMP-compliant, and the production process itself may not be scalable to desired output levels.

Notwithstanding the availability of immunocompetent polymers for nanoparticle surface modification aimed at prolonging circulation time [51], there may be more effective and more practical routes to (targeted) PS delivery that are clinically feasible. In this study, bionanovesicles were prepared from tumor cells by simple sonication and loaded with ZnPC for PDT of cultured human extrahepatic cholangiocarcinoma (TFK-1) cells. The bionanovesicles were termed cellular vesicles (CVs; vesicles prepared by sonication of tumor cells without prior cell content removal) and cell membrane vesicles (CMVs; vesicles prepared by sonication of tumor cells with prior cell content removal). The CVs and CMVs are fundamentally distinct from secreted or actively formed extracellular vesicles, which entail exosomes, microvesicles, and apoptotic bodies, that have been widely studied for purposes of drug delivery [52] and to some degree for PS delivery [53]. In contrast, the bionanovesicles were prepared by physically perturbing cells and structurally rearranging the cellular constituents, yielding nanovesicles with different intravesicular content, bilayer composition, and membrane surface architecture. This approach has not been investigated in the context of PS delivery and PDT. The CVs and CMVs were therefore studied in terms of ZnPC encapsulation efficacy, photosensitization potential of TFK-1 cells, dark toxicity, and photodynamic potency in TFK-1 cell monolayers. The main objectives of this first-in-its-class proof-of-concept study were to rule out cytotoxicity of the PS-encapsulating bionanovesicles and assess the level of phototoxicity in comparison to liposomal photonanomedicines.

2. Results and Discussion

Supplemental material is designated with prefix 'S' and the section numbering in the supplemental material corresponds to that in the main text. A list of abbreviations is also provided in the supplemental material. Sample sizes are provided in the figure legends.

2.1. Rationale for Using CVs and CMVs for ZnPC Delivery into Tumor Cells

Inasmuch as extracellular vesicles play an important role in intercellular signaling [54], and as such these vesicles are taken up by cancer cells, our initial efforts were directed towards exosomes as vehicles for ZnPC delivery into cholangiocarcinoma cells. ZnPC was chosen to enable comparison to our previous studies with liposomal formulations [7–9,11,12,19,30,32]. Conceptual validation in regard to loading of different PSs into exosomes had already been performed with ZnPC [55,56], chlorin e6 [57–59], tetrasulfonated aluminum phthalocyanine [60], protoporphyrin IX [61], DCPy [62], and Rose Bengal [63]. Also, a plethora of exosome sources had been explored, such as blood [61], urine [57], milk [56], immune cell subsets [56,59,64,65], tumor cells [55,56,58,60,62], and immortalized primary cells [63]. It was opted to use TFK-1 cells as the source of exosomes, which were enumerated via ultracentrifugation [66] and by means of a commercial kit (ExoSpin, Cell Guidance Systems, St. Louis, MO, USA) [55,67–69].

The yield of exosomes relative to the number of cells required was roughly 4 orders of magnitude lower than that of bionanovesicles. A batch of 10^7 TFK-1 cells (roughly 1 T175 cell culture flask) produced 127 ng of exosomes versus 0.8 mg of CMVs based on protein content, with EVs and CMVs being comprised of approximately the same amount of protein per unit phospholipids (0.7 μmol phospholipids/mg protein and 1.7 μmol phospholipids/mg protein, respectively). CV quantitation was omitted in these measurements because TFK-1 intracellular proteins were not removed from the suspension. Compared with CMVs and especially CVs, the preparation and isolation methods for extracellular vesicles are considerably more tedious [53] and less cost-effective and likely constitute a hurdle to eventual large scale GMP production.

For these reasons, and the fact that native cell membrane-based nanoparticulate drug delivery systems were shown to benefit tumor cell targeting [55,70–73], it was decided to develop and test a new biomimetic PS delivery system.

2.2. CVs and CMVs Exhibit Useful Physicochemical Properties for PS Delivery

The mean ± SD particle size of CVs and CMVs was 134.3 ± 0.9 nm and 172.1 ± 3.2 nm, respectively (Fig. 2A). These dimension are comparable to ZnPC-encapsulating ITLs [7,12,19], endothelium-targeting liposomes (ETLs) [10], and tumor cell-targeting liposomes [32]. Compared with larger particles, this size range was shown to be most abundantly taken up by tumor cells in regard to PEGylated liposomes [7]. The particle diameters are also ideal for in vivo applications in terms of circulation time, at least if the CVs and CMVs conform to the pharmacokinetics of PEGylated liposomes, which should be between 136 and 220 nm for minimal hepatic clearance, moderate splenic uptake, and maximal circulation time [74]. PEG mimicry by bionanovescicles emanates from the tumor cell glycocalyx, a layer of multifunctional glycans that covers the surfaces of cancer cells [75,76], which was retained in CVs and CMVs. The glycocalyx functions as a steric barrier to cell-cell interactions [77] and hence emulates the properties of liposome surface-grafted PEG [78,79]. The mean ± SD polydispersity index (PDI) values for CVs and CMVs were 0.220 ± 0.013 and 0.167 ± 0.022, respectively, and reflect a diametrically homogeneous population of vesicles (cutoff at <0.3) [80]. The zeta potentials were − 16.1 ± 0.9 mV and − 16.4 ± 1.1 mV for CVs and CMVs, respectively (Fig. 2A). The anionic surface probably stems from particular glycocalyx constituents, namely the sialic acid-rich glycans, replete on the tumor cell membrane [76]. A negative surface charge is typically associated with accelerated nanoparticle internalization by tumor cells [7,81]. However, since endocytic cells such as macrophages also have a predilection for anionic particles [82], particularly when the surface meshwork also contains embedded opsonins [83], the balance between RES clearance and tumor targeting will have to be appraised in an in vivo setting.

Further investigation involved the stability of CVs and CMVs during a 1-wk storage period and in the presence of various organic solvents, including DMSO, methanol, ethanol, and pyridine. The latter experiments were performed in anticipation of loading drugs, including ZnPC, into the bionanovesicles. The presence of organic solvent molecules may perturb biomembrane stability and cargo retention. Stability was gauged by size and PDI determination using photon correlation spectroscopy. It should be noted that these experiments centered on early-phase development and testing, as the use of organic solvents such as pyridine will be removed from the bionanovesicle production process for the in vivo testing stage [84].

During cold storage for 1 wk, the CVs and CMVs increased in diameter to 178 ± 4 nm (PDI = 0.176 ± 0.002) and 250 ± 10 nm (PDI = 0.355 ± 0.178), respectively (data not shown), corresponding to a relative size increase of 33% and 45%, respectively. The measurements indicate that the bionanovesicles mildly aggregate, which was not observed for e.g., PEGylated third-generation ZnPC-ETLs and fourth-generation ZnPC-ETLs that co-encapsulate the HIF-1α and topoisomerase inhibitor acriflavine during the course of 14 d [10].

The addition of 1–30% *v*/v pyridine, which has been our standard solvent for ZnPC [7–12,19], exerted no notable effect on bionanovesicle diameter but caused a gradual increase in PDI with concentration (Fig. 2C, D). The effect of DMSO, ethanol, and methanol was also determined given that these solvents are often used to dissolve drugs. CMVs were more susceptible to the solvents than CVs, and both types of bionanovesicles exhibited the highest sensitivity towards ethanol and more or less equal sensitivity towards DMSO and methanol. Destabilization effects were generally solvent concentration-dependent. Accordingly, the solvent system should be taken into consideration

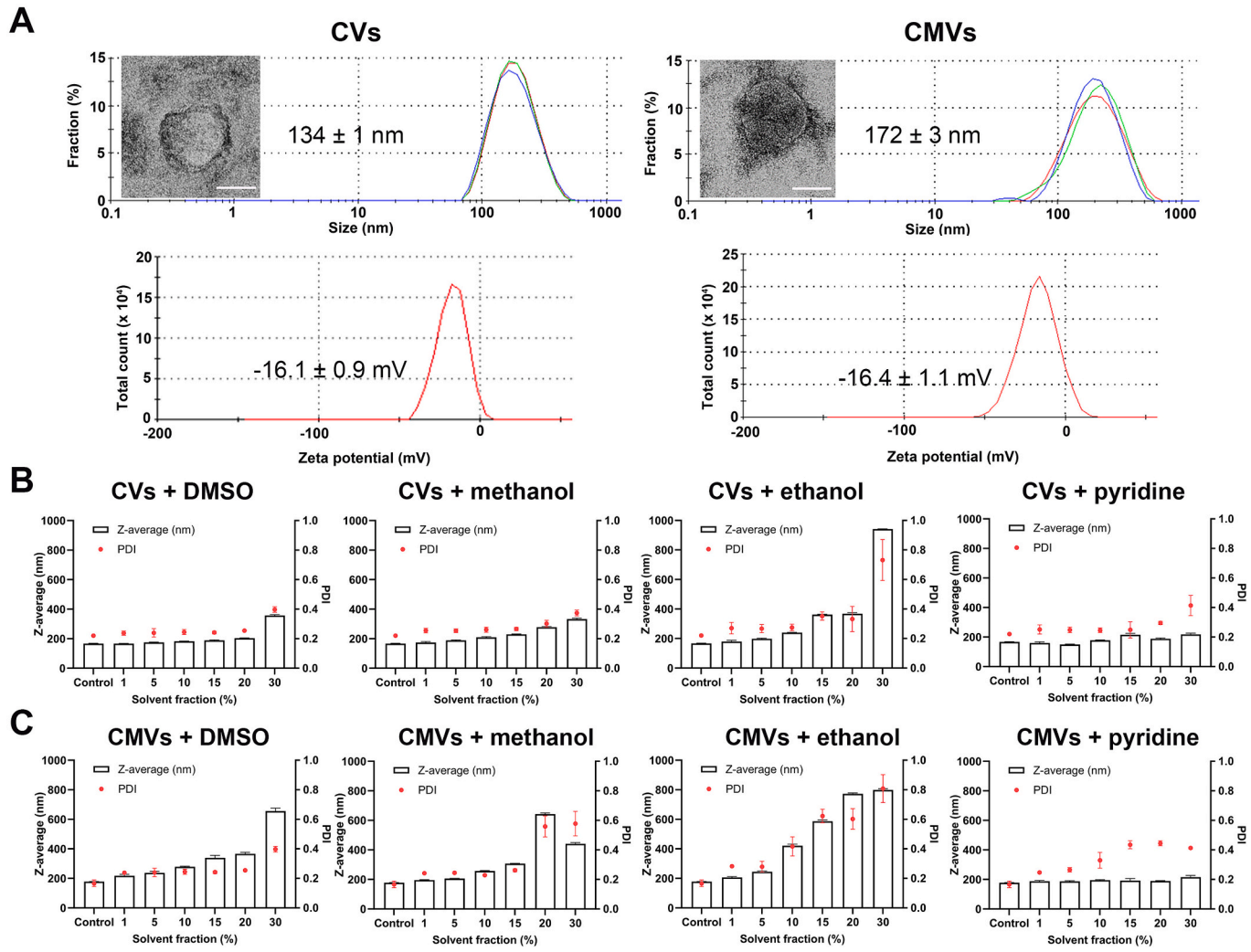

Fig. 2. Physicochemical characterization of CVs and CMVs and the effect of various solvents on nanoparticle stability. (A) Bionanovesicle diameter (top row) and zeta potential (bottom row). Size-related values represent mean ± SD of 3 repeated measurements (traces top row). The inserts show representative TEM images of a CV and CMV (scale bar, 100 nm). Influence of increasing concentrations of DMSO, ethanol, methanol, and pyridine on CV (B) and CMV stability (C) as measured by photon correlation spectroscopy and expressed as mean ± SD size (left *y*-axis, bars) and polydispersity index (PDI; right *y*-axis, dots). Data represent $N = 3$/group.

during the drug loading process in cases where the aqueous and organic solvent systems are mixed and desiccation (e.g., lyophilization, evaporation [7,12,19]) is not part of the preparation protocol, as was the case in this study to preserve tumor cell membrane integrity. We have shown previously that DMSO, ethanol, and methanol become toxic to cultured hepatocytes (AML-12, HepG2, and HepaRG) at a concentration of ≥3% (*v*/v) [85], which should also be accounted for in the experimental design.

2.3. *ZnPC Is Effectively Loaded into Bionanovesicles by Solvent Mixing and Sonication, but Only up to a Maximum ZnPC:Phospholipid Ratio*

The next step was to load ZnPC into bionanovesicles by addition of ZnPC in pyridine to the CVs in 10 mM HEPES, pH = 7.5, solution and the CMVs in MilliQ water, followed by tip sonication to facilitate ZnPC entry into the biomembranes. There was a PS concentration-dependent moderate increase in ZnPC-CV and ZnPC-CMV diameter and PDI (Fig. 3A and B), of which the former was likely caused by the ZnPC instead of the pyridine when juxtaposed to Fig. 2B and C. Nevertheless, even at the highest ZnPC loading ratio the particle diameter remained within the ideal range for in vivo applications (section 2.2). However, when the amount of added ZnPC was compared to actual (measured) ZnPC using Bland-Altman analysis [86], a divergence was observed when >2.7 μM of ZnPC was added to CVs composed of 500 μM phospholipids (0.006 PS:phospholipid ratio) (Fig. 3C) and when >4.5 μM of ZnPC was added to CMVs standardized to 500 μM phospholipids (0.01 PS:phospholipid ratio) (Fig. 3D). The loss of PS was attributed to ZnPC aggregation and segregation from the bionanovesicle membrane after solvent mixing to a predominantly aqueous environment and subsequent removal of the ZnPC aggregates from the batch during preparation; a phenomenon that was also observed for ZnPC-ITLs [7]. Sedimentation of blue aggregates was confirmed by visual inspection (not shown). In practice this translates to plateauing of the photosensitization potential of the nanocarrier system because it caps the amount of PS molecules that can be delivered to tumor cells per nanoparticle, which places some restrictions on PDT efficacy.

Based on the absorption spectra of ZnPC-CVs (Fig. 3E) and ZnPC-CMVs (Fig. 3F), it became clear that extrananoparticulate ZnPC aggregation and intramembrane dimer-/multimerization are not mutually exclusive and concurred at similar PS:phospholipid ratios. ZnPC dimer-/multimerization has been spectroscopically demonstrated in liposomal formulations at ZnPC:lipid ratios above 0.003 (DPPC) [7], 0.007 (DMPC) [87], and 0.013 (POPC:DOPS) [84,88]. Interactions with the chemical milieu (solvent molecules, pH, phospholipid acyl chains,

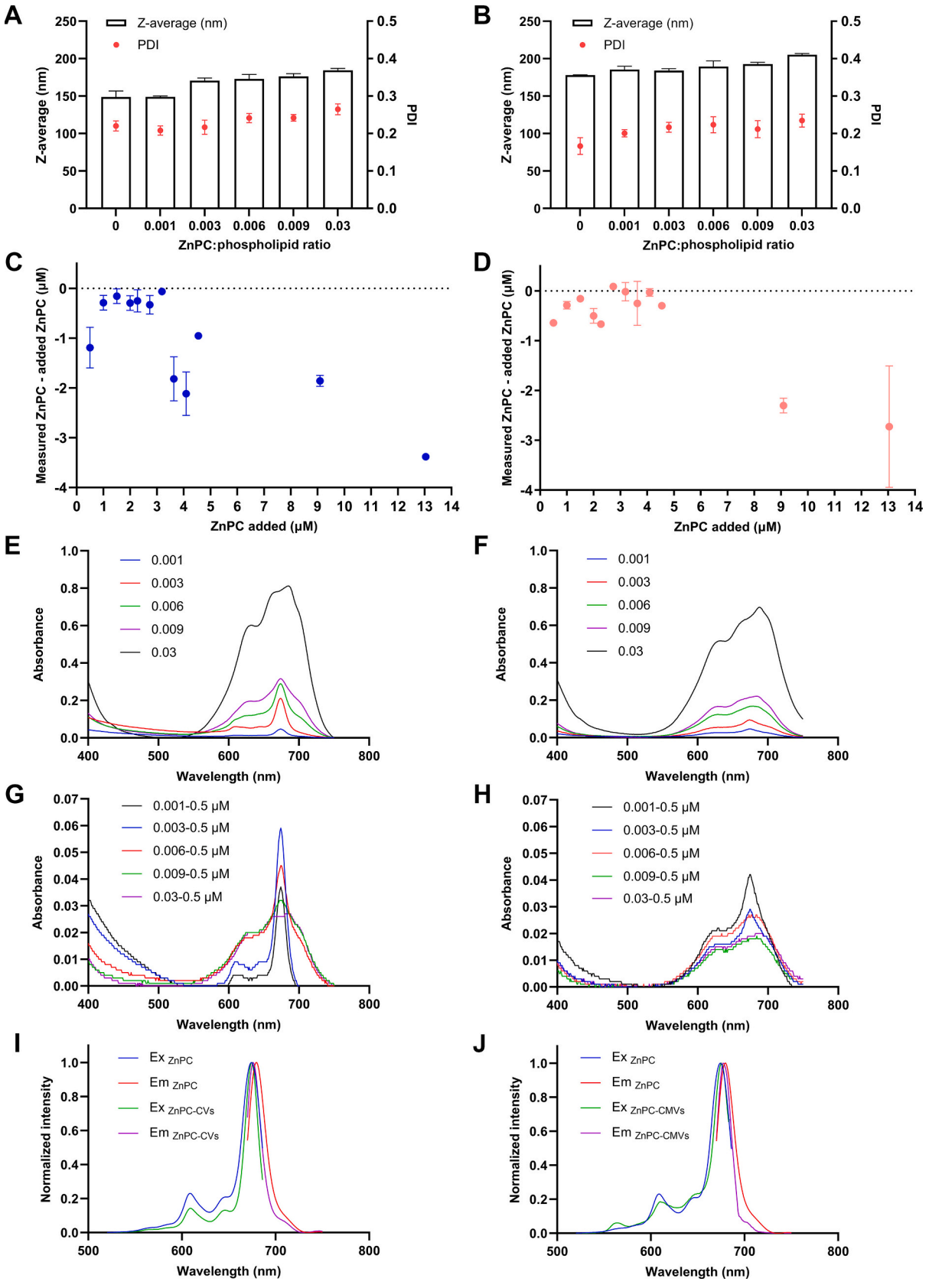

(caption on next page)

Fig. 3. Spectral and physicochemical properties of ZnPC-CVs and ZnPC-CMVs. (A, B) Particle sizes of ZnPC-CVs and ZnPC-CMVs at a fixed 500-μM phospholipid concentration and 0.001–0.03 ZnPC:phospholipid molar ratios. Data represent mean ± SD of $N = 3$ measurements per group. The pyridine volume fraction was 10% for bionanovesicles with a ZnPC:phospholipid ratio range of 0.001–0.009 and 15% for bionanovesicles with a ZnPC:phospholipid molar ratio of 0.03. Bland-Altman plot of the nominal differences (*y*-axis, in μM) between the measured amount of ZnPC and the added amount of ZnPC in CVs (C) and CMVs (D) at 500-μM phospholipid concentration and 0.001–0.03 ZnPC:phospholipid molar ratios. The difference was calculated by (measured ZnPC - added ZnPC) and plotted per added ZnPC amount in pyridine (μM) to the bionanovesicle mixture (*x*-axis). Bionanovesicular ZnPC concentrations were determined spectrophotometrically against a standard curve. Absorption spectra of ZnPC-CVs (E) and ZnPC-CMVs (F) at a fixed 500-μM final phospholipid concentration and 0.001–0.03 ZnPC:phospholipid molar ratios. (G, H) Absorption spectra of ZnPC-CVs and ZnPC-CMVs at a fixed 0.5-μM ZnPC concentration and increasing ZnPC:phospholipid molar ratios (0.001–0.03). Normalized fluorescence excitation (Ex) and emission (Em) spectra of 1.5 μM ZnPC in pyridine and an equimolar amount of ZnPC encapsulated in CVs (I) and CMVs (J) (0.003 ZnPC:phospholipid ratio, 500-μM final phospholipid concentration).

transmembrane proteins, etc.) as well as any form of bonding (e.g., dimerization) affects the ground states within the delocalized system of metallated phthalocyanines, which manifests spectroscopically as peak shifts, appearance of shoulders [89], and Q-band splitting [90–92]. In terms of the type of aggregation, it is believed that ZnPC forms H-aggregates in biomembranes as opposed to J-aggregates. H-aggregates are formed by molecular face-to-face stacking, while J-aggregates form by molecular head-to-tail arrangement [93]. Our unpublished molecular dynamics studies on the orientation of ZnPC in biomembranes revealed that ZnPC inserts iteself parallel to the bilayer normal, a configuration that would preclude J-aggregate formation due to the increased polarity at the phospholipid backbone and head group surface on both ends of phospholipid bilayer [94].

With respect to CVs, shifts from the 674-nm Q-band peak [95] only occurred in ZnPC-CVs at a 0.03 ZnPC:phospholipid ratio (at fixed phospholipid concentration, bathochromic shift to 685 nm; at fixed ZnPC concentration, bathochromic shift to 684 nm; Fig. 3E and G, respectively). Q-band splitting in the absorption peak and shoulder development was exacerbated in CVs formulated at a 0.03 ZnPC:phospholipid molar ratio (Fig. 3E). Spectral deformation started with the appearance of a red shoulder around 710 nm (0.006 ZnPC:phospholipid molar ratio) and the convergence of the two minor Q-bands at ~610 and ~ 650 nm into a new minor Q-band at ~630 nm (0.009 ZnPC:phospholipid molar ratio) (Fig. 3E).

In regard to CMVs, a bathochromic drift from the Q-band maximum was observed at increasing ZnPC:phospholipid ratios in both instances (at fixed phospholipid concentration, main Q-band absorption peaks at 674 nm (ZnPC:phospholipid ratio of 0.001 and 0.003), 676 nm (0.006), 681 nm (0.009), and 685 nm (0.03); at fixed ZnPC concentration, absorption peaks at 674 nm (ZnPC:phospholipid ratio of 0.001 and 0.003), 675 nm (0.006), 684 nm (0.009), and 687 nm (0.03); Fig. 3F and H, respectively). The absorption spectra were structureless at all ZnPC:phospholipid ratios, particularly at the higher ratios, indicating strong chemical effects of the biomembrane environment on ZnPC electronic states.

ZnPC absorption spectra were restored in both CVs and to some extent CMVs to their 'native' ground state absorption spectra (both in organic solvent and liposomal membranes [7,12,19,20]) when the phospholipid concentration was increased at constant ZnPC content (5 μM; Fig. 3G and H, respectively), suggesting that intramembrane ZnPC aggregation is a factor at higher ZnPC:phospholipid ratios. Despite the deleterious effects of intramembrane PS aggregation on ROS production and (bio)molecule oxidation in nanoparticles [7], dimer/multimerization inside the CVs and CMVs is inconsequential to PDT efficacy inasmuch as nanoparticle-delivered ZnPC is homogenously dispersed throughout the lipophilic compartments of a (tumor) cell after internalization [12,19] and resides in monomeric state due to dilution effects.

Finally, the fluorescence emission and excitation spectra were recorded of ZnPC-CVs (Fig. 3I) and ZnPC-CMVs (Fig. 3J) at a ZnPC:phospholipid ratio of 0.003 and juxtaposed to ZnPC in pyridine. ZnPC in pyridine exhibited an emission maximum at 679 nm and an excitation maximum at 674 nm, which are consistent with previously published data [7,19]. The fluorescence emission maxima of CV- and CMV-encapsulated ZnPC were hypsochromically shifted, but not to a significant extent (2 nm for ZnPC in CVs; 1 nm in ZnPC in CMVs). The excitation spectrum of CV-encapsulated ZnPC did not differ notably from that of ZnPC (Fig. 3I) and was superimposable on the absorption spectrum of free ZnPC in pyridine [7,95] and CV-encapsulated ZnPC up to a ZnPC:phospholipid ratio of 0.003 (Fig. 3G). The same applied to the excitation spectrum of ZnPC in CMVs.

Taken together, fluorescence-based assays with ZnPC-containing CVs and CMVs are not expected to be affected spectrally despite the anomalous absorption spectra indicative of quantum-level perturbations. However, the spectral shifts as well as the intramembrane aggregation make quantitative spectroscopic analysis impossible for intact CVs and CMVs. Equally, in vitro investigations on the extent of ROS production by the bionanovesicles created at higher ZnPC:phospholipid ratios will skew the results in that ROS production is dampened by the PS stacking. This does not preclude the fabrication of CVs and CMVs at higher ZnPC:phospholipid ratios for in vitro and in vivo PDT applications on the condition that the PS disperses throughout the cell (Fig. S1) following bionanovesicle internalization [10]. Of note, internalization of nanoparticle-delivered ZnPC does not always concur with homogenous PS dispersion throughout the cell following uptake; a phenomenon that may affect PDT efficacy [96].

2.4. *Bionanovesicles Improve Delivery of ZnPC into Cultured Cholangiocarcinoma Cells, which Become Homogeneously Photosensitized*

For proper photosensitization, the delivery vehicle carrying the PS must be internalized by the target cells. To that end, association between bionanovesicles and cells was tested first by flow cytometry as a preliminary screening method. TFK-1 cells were incubated with ZnPC-CVs, ZnPC-CMVs, or an equimolar concentration of free ZnPC and association was probed by exploiting ZnPC's intrinsic fluorescence (Fig. 3I and J). As shown in Fig. 4A, ZnPC-CVs and ZnPC-CMVs associated with TFK-1 cells, the extent of which correlated positively with incubation time. Based on fluorescence intensity, the association was stronger when ZnPC was introduced to cells in bionanovesicles rather than in non-encapsulated form. Given that free ZnPC enters the cell membrane, which is similar to its location in TFK-1 cell-derived CVs and CMVs, the fluorescence intensities can be compared across platforms. The level of nanoparticle-cell association was indiscriminate between CVs and CMVs and directly proportional to the ZnPC:phospholipid ratio (Fig. 4B and C).

Following flow cytometry, confocal microscopy was performed to determine whether the association comprised uptake and to investigate the temporal kinetics of intracellular distribution of ZnPC. Whereas free ZnPC became visible at the 30-min incubation time point (Fig. 4D), TFK-1 cells were replete with ZnPC delivered by CVs (Fig. 4E) and CMVs (Fig. 4F) already after 15-min incubation. The fluorescence intensity in the red channel (ZnPC) did not remarkably increase at subsequent time points, indicating that a saturation level was reached rapidly ensuing cell exposure to the bionanovesicles. Rapid uptake of CVs and CMVs may be related to their surface properties and structural mimicry of EVs [97] and apoptotic bodies [98], which are designed to be taken up to facilitate intercellular signaling [99] and expose phosphatidylserine on the outer membrane leaflet that serves as an 'eat me' signal [100], respectively. The sonication step rearranges the (phospho)lipid packing order in biomembranes, which may for instance abet the exposure of

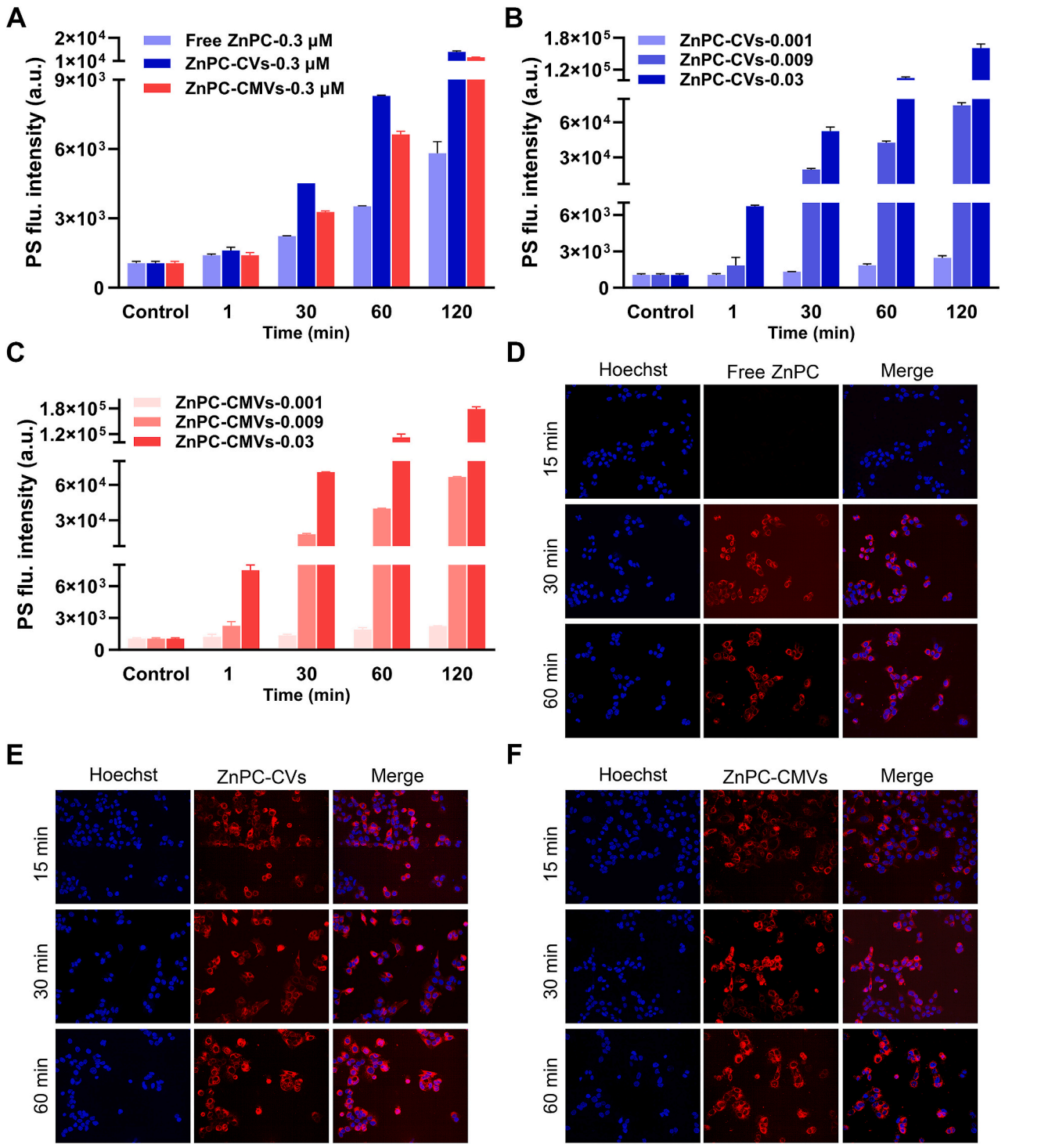

Fig. 4. Association, uptake, and intracellular distribution of free ZnPC, CV-delivered ZnPC, and CMV-delivered ZnPC in TFK-1 cells. (A) TFK-1 cells were incubated with 0.3 μM ZnPC in pyridine or an equimolar amount of ZnPC encapsulated in CVs and CMVs (0.003 ZnPC:phospholipid ratio) for 1–120 min and analyzed by flow cytometry. The mean ZnPC autofluorescence intensity is plotted as a function of incubation time ($N = 3$ per time point). (B, C) TFK-1 cells were incubated with ZnPC-CVs or ZnPC-CMVs at a fixed 100-μM final phospholipid concentration and 0.001–0.03 ZnPC:phospholipid molar ratios for 1–120 min and analyzed by flow cytometry. The mean ZnPC autofluorescence intensity is plotted as a function of incubation time (N = 3 per time point). (D, E, and F) TFK-1 cells were incubated with 3 μM ZnPC in pyridine or an equimolar amount of ZnPC encapsulated in CVs and CMVs (0.003 ZnPC:phospholipid ratio) for 15–60 min and imaged by confocal microscopy (ZnPC, red fluorescence). Hoechst 33342 (blue fluorescence) was used to stain DNA. (For interpretation of the references to colour in this figure legend, the reader is referred to the web version of this article.)

phosphatidylserine and aid in the accessibility of transmembrane- or membrane-anchored proteins that mediate cellular uptake [101–104]. Future in vivo investigations will reveal whether the use of these bio-nanovesicles is favorable in terms of pharmacokinetics and tumor targeting.

ZnPC distributed homogenously throughout the cell but without entering the nucleus (Fig. S1), which is comparable to free ZnPC in other cell lines (e.g., A549 [105] and PC3 [106]) as well as protein-delivered

ZnPC in PC3 cells [106], liposome-delivered ZnPC in various cell lines (A431, SK-ChA-1, RAW 264.7, NIH-3 T3, and HUVECs) [12,19], and micelle-delivered ZnPC in MCF-7 cells [107]. With this pattern of localization across numerous organelles, it is expected that PDT will trigger multiple modes of cell death executed through a number of different pathways and therefore increase relative lethality [20] and minimize chances of recovery [22].

2.5. ZnPC-CVs and ZnPC-CMVs Are Not Toxic to Cultured Cholangiocarcinoma Cells

A key criterion for clinically safe PDT is that the PS as well as its delivery vehicle are inherently non-toxic [108], which is why dark toxicity experiments were conducted where TFK-1 cells were incubated with bare and PS-loaded CVs and CMVs in the absence of illumination. Viability was assessed over a time span of 3 d [12,19] using the MTS assay.

Neither CVs nor CMVs induced any toxicity in TFK-1 cells up to a final phosphospholipid concentration of 500 μM and 3-d exposure (Fig. 5A), although 3-d incubation with CMVs had a slight toxic tendency. TFK-1 cells exposed to free ZnPC (0–1.5 μM final concentration) exhibited no dark toxicity regardless of incubation time (Fig. 5B, green bars), which is consistent with earlier reports on DPPC liposome-delivered ZnPC in other cell lines [7,9,12,19]. TFK-1 cells subjected to up to 1.5 μM ZnPC in CVs (Fig. 5B, blue bars) and CMVs (Fig. 5B, red bars) (500-μM final phospholipid concentration) exhibited no notable consequences on viability. These data attest to an absence of dark toxicity from the ZnPC as well as ZnPC-CVs and ZnPC-CMVs, at least in tumor cell monolayer cultures.

2.6. PDT of CV- and CMV-Photosensitized Cultured Cholangiocarcinoma Cells Exacts Nanomolar-Range ZnPC Concentrations to Achieve Half-Maximum Lethality

In the final analysis, TFK-1 cells photosensitized with ZnPC, ZnPC-CVs, and ZnPC-CMVs were subjected to PDT and screened for viability at 24 h, 48 h, and 72 h after treatment using the MTS assay. In the first test arm, cells were primed with ZnPC up to a final concentration of 1.5 μM (at a fixed ZnPC:phospholipid ratio of 0.003). In the second test arm, the phospholipid concentration in medium was fixed at 100 μM while bionanovesicular ZnPC content was varied (0, 0.1, 0.6, 0.9, and 3 μM).

The most important findings were that (1) PDT efficacy proceeded in the order of ZnPC-CMVs > ZnPC-CVs > ZnPC for all time points and that (2) PDT-mediated cytotoxicity increased with incubation time for ZnPC and ZnPC-CVs but not ZnPC-CMVs (Fig. 6A-C). Both phenomena are reflected in the LC_{50} values derived from the fit functions (Fig. 6D), which show a decreasing trend with incubation time for free and CV-encapsulated ZnPC. In terms of ZnPC-CMVs, it is currently not known why cell death is already profound at the earliest measurement time (24 h post-PDT) while the execution of cell death pathways continues during a longer time course for free and CV-delivered ZnPC and ultimately results in less toxicity. CMVs may saturate cells with oxidation-prone phospholipids that, at physiologically precarious locations (cell and subcellular membranes) for which cells do not possess enzymatic redox protection [109], facilitate cascading membrane damage that leads to perturbation of cellular homeostasis that in turn culminates in various forms of cell death [110]. This is particularly important for membrane-intercalating PSs such as ZnPC (logP of 8.5) that generates predominantly singlet oxygen [20], which is very reactive towards olefinic bonds in the phospholipid acyl chains [111]. CVs, on the other hand, may deliver protective components to tumor cells insofar as these bionanovesicles still embody cellular content, possibly offsetting the exacerbated PDT-induced membrane damage facilitated by CMVs.

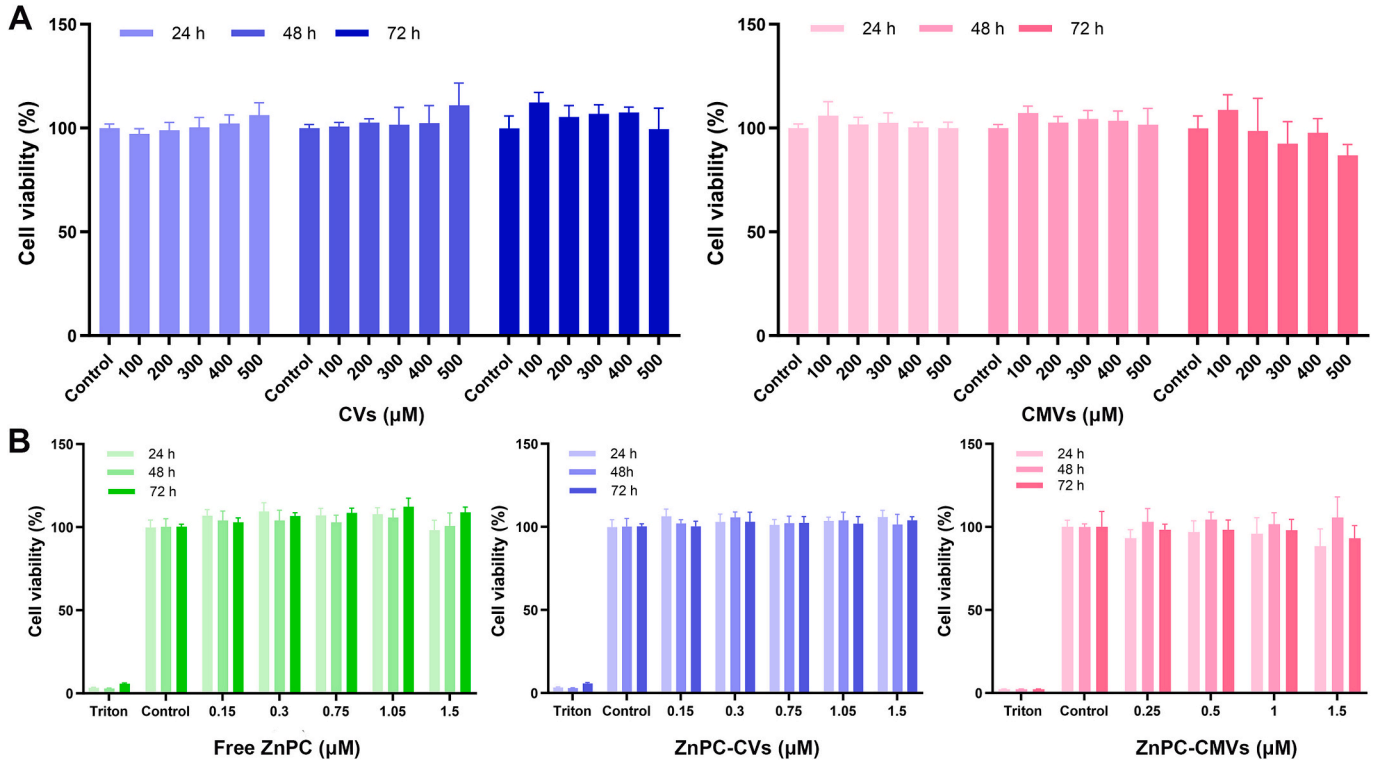

Fig. 5. (A) In vitro dark toxicity of free ZnPC, ZnPC-CVs, and ZnPC-CMVs and (B) toxicity of CVs and CMVs in TFK-1 cells. TFK-1 cells were incubated with free ZnPC, ZnPC-CVs, and ZnPC-CMVs (0–1.5 μM final concentration) in $RPMI^{-/-}$ medium and maintained under standard culture conditions for 24 h, 48 h, and 72 h. Cell were assayed by the CellTiter-96 AQ ONE assay. Data ($N = 8$ per concentration per time point) were normalized to the control group mean.

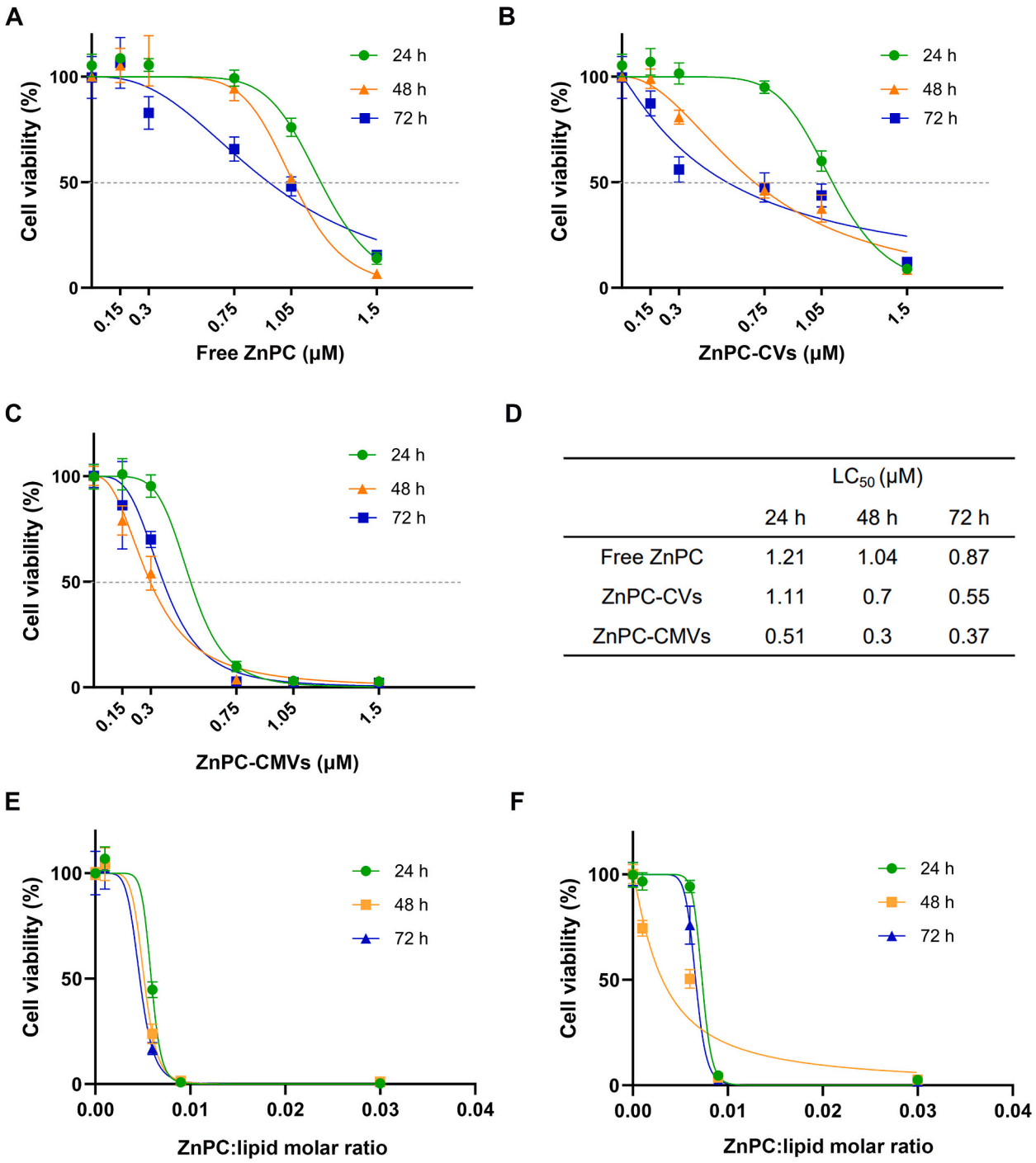

	LC_{50} (μM)		
	24 h	48 h	72 h
Free ZnPC	1.21	1.04	0.87
ZnPC-CVs	1.11	0.7	0.55
ZnPC-CMVs	0.51	0.3	0.37

Fig. 6. PDT-induced cell death as a function of ZnPC concentration. TFK-1 cells were incubated for 1 h with free ZnPC (A), ZnPC-CVs (B), or ZnPC-CMVs (C) (ZnPC:phospholipid ratio of 0.003) and washed directly before PDT, which was performed at a cumulative radiant exposure of 35.3 J/cm^2. Cell viability of TFK-1 cells treated with free ZnPC was assessed by the CellTiter-96 AQ ONE assay at 24 h, 48 h, and 72 h post-PDT ($N = 8$ per PS concentration). PS incubation and post-PDT cell culture were performed in RPMI$^{-/-}$ medium under standard culture conditions. Results were normalized to the mean value of the control group (medium only, cumulative radiant exposure of 35.3 J/cm^2). (D) Calculated LC_{50} values classified per PS group and per post-PDT incubation time. Cell viability of TFK-1 cells photosensitized with ZnPC-CVs (E) and ZnPC-CMVs (F) at different ZnPC:phospholipid ratios and 100-μM final phospholipid concentration. Viability was assessed as described above (cumulative radiant exposure of 35.3 J/cm^2; N = 8 per group). PS incubation and post-PDT recovery were performed in RPMI$^{-/-}$ medium under standard culture conditions. Results were normalized to the mean value of the control group (medium only + illumination).

It was further demonstrated that the ZnPC concentration range in which temporal differences in the degree of cell death are manifest lies between a ZnPC:phospholipid ratio of 0.001 (lower bound) and 0.009 (upper bound) in cultured cell monolayers (Fig. 6E and F). At the lower bound there was 100% viability after PDT whilst beyond the upper bound there was 100% cell death. Based on phospholipid measurements and confluence level at the point that cells were subjected to PDT, each well contained roughly 9.5×10^{-4} μg of cellular phospholipids ($\sim 3.8 \times 10^{-8}$ μg/cell) and received 7.44 μg of phospholipids from CVs/CMVs. Correspondingly, the amount of CV/CMV-delivered ZnPC added to a well at 0.001 ZnPC:phospholipid ratio (lower bound) was 2.9×10^{-4} μg, accounting for a ZnPC:TFK-1 phospholipid ratio of

approximately 0.3. This ratio discounts the CV/CMV phospholipids taken up by cells along with the PS. At the upper bound, i.e., a ZnPC: phospholipid ratio of 0.009, the amount of delivered ZnPC was 2.6×10^{-3} μg, which accounted for a ZnPC:TFK-1 phospholipid ratio of approximately 2.7. Given that at a ZnPC:phospholipid ratio of 0.003 the extent of redox probe and biomolecule oxidation plateaus due to triplet state deactivation following ZnPC dimer-/multimerization in biomembranes [7], it may be assumed that at a ZnPC:bionanovesicular phospholipid ratio of 0.009 (Fig. 6E and F) a state of maximum ROS production and destruction had been reached. Following that assumption and the fact that the degree of cell death is proportional to ROS production, which in turn is proportional to the amount of intracellular PS levels, a ZnPC:bionanovesicular phospholipid ratio of 0.006 that yielded about 55–85% cell death (Fig. 6E and F) is most likely associated with ZnPC residing in monomeric state after TFK-1 cell entry. This supposition therefore implies that, of the total amount of added ZnPC (1.7×10^{-3} μg for the 0.006 ZnPC: bionanovesicular phospholipid ratio) to a total of 9.5×10^{-4} μg of cellular phospholipids, approximately 2.9×10^{-6} μg of ZnPC molecules had entered the TFK-1 cells. Taken together, these calculations imply that slightly >1‰ of CVs/CMVs are endocytosed during the 1-h incubation period at standard culture conditions.

Finally, the LC_{50} values obtained in this study were compared to results obtained in other studies on ZnPC-encapsulating liposomes (Table 1). The ZnPC LC_{50} values range from 0.03 μM [11] to >16 μM [112] (mean ± SD of 3.2 ± 4.4 μM) regardless of post-PDT incubation time and from 0.13 μM [19] to >16 μM [112] (mean ± SD of 4.1 ± 5.1 μM) for the 24-h post-PDT time point. The LC_{50} values obtained with ZnPC-CVs (1.11 μM, 24 h) and ZnPC-CMVs (0.51 μM, 24 h) mark the lower end of the LC_{50} spectrum and attest to the potent phototoxicity of the ZnPC-loaded bionanovesicles compared to liposomal PS delivery systems, at least when predicated on in vitro data. Naturally, the LC_{50} values in this comparison framework should be properly contextualized insofar as these values are impacted by factors such as cumulative radiant exposure, cell line, and culture conditions that have not been standardized across the included studies. Nevertheless, ZnPC-encapsulating bionanovesicles as PS delivery system constitute an appealing approach that warrants further testing beyond in vitro conditions.

2.7. Caveats and Future Directions

Although the data presented are encouraging, several important caveats should be mentioned. First, the study concerns in vitro work only, and the translation to the ultimate application (in patients) may be lost due to the inherent obstacles often encountered during the transit to animal studies (e.g., pharmacokinetics, immune system, physiology) and subsequently humans (fundamental interspecies differences) [113]. Second, it is difficult to anticipate how a living organism's immune system will respond to nanoparticles composed of membranes and associated surface structures derived from cultured cancer cell lines. Normally, innate and adaptive immune system cells have sensitive detection and elimination machinery that will lead to nanoparticle clearance and hence suboptimal tumor photosensitization. Third, a protocol will need to be developed for the loading of ZnPC into bionanovesicles that does not involve potentially harmful organic solvents (e.g., pyridine) for living organisms. Fourth, oxygenation is no issue in cell culture monolayers while in three-dimensional tumors with peripheral cell hyperproliferation and hypovascularization matters such as PS delivery (particularly in case of highly hydrophobic PSs) and hypoxia may be problematic and deleterious to therapeutic efficacy. The next steps should therefore focus on formulating physiologically compatible PS-carrying bionanovesicles and providing in vivo proof-of-concept with strong emphasis on pharmacodynamics (PDT efficacy) as well as systemic and skin phototoxicity [12].

3. Conclusions

This first-in-its-class study showcased the utility of tumor cell-derived bionanovesicles for the encapsulation of a hydrophobic PS and subsequent PS delivery into the same cells that had been used as source material for the bionanovesicles. Two types of bionanovesicles were formulated; CVs composed of whole cell material and CMVs comprising isolated cell membranes, and loaded with ZnPC. Both CVs and CMVs conformed to physicochemical properties aspired for optimal in vivo drug delivery. The bionanovesicles exhibited no dark toxicity in cultured tumor cells and were taken up to photosensitize target cells in a homogenously dispersive manner. PDT yielded low-to-subnanomolar range LC_{50} values that easily compete with liposomal ZnPC delivery systems. Follow-up studies will need to evince in vivo suitability, absence of toxicity, and effective tumor targeting as well as therapeutic potency.

4. Materials and Methods

The chemicals/compounds, buffers, and reagents/kits are summarized in Table S1. Equipment and materials/disposables are listed in Table S2. Cells and cell culture-associated paraphernalia are summarized in Table S3. The concentrations listed are final unless specified otherwise. All procedures involving PSs were performed under dim light conditions.

4.1. Photosensitizer, Phospholipids, and Buffers

For the loading of exosomes and bionanovesicles, ZnPC was dissolved in pyridine at a 100-μM stock concentration. ZnPC stock solutions were stored under a nitrogen atmosphere at room temperature (RT) in the dark. Phospholipids (Table S1) were dissolved in chloroform and stored under a nitrogen atmosphere at −20 °C.

4.2. Cell Culture

Cell lines are routinely screened (every 3 m) for mycoplasma infection (MycoAlert Mycoplasma Detection Assay, Lonza) at the Department of Pharmaceutics, Utrecht University, where this work was performed. The cells described in this study were mycoplasma-free and cultured in a dedicated mycoplasma-free facility.

4.2.1. Cell Culture for CV and CMV Production

TFK-1 cells (human extrahepatic biliary adenocarcinoma) were cultured in T75 flasks and subsequently in T175 flasks in phenol red-containing RPMI 1640 medium supplemented with 10% fetal bovine serum (FBS) but without antibiotics or addition L-glutamine. The cells were grown under standard culture conditions (dark, 37 °C, humidified atmosphere composed of 5% CO_2 and 95% air) and subcultured twice per week at a ratio of 1:14 to maintain a logarithmic growth phase at all stages. Subculturing was performed before reaching 90–95% confluence, assessed with a brightfield microscope.

For subculturing and collection, cells were washed twice with PBS (RT, 10 mL/T75 flask and 25 mL/T175 flask) prior to detachment using vacuum aspiration and incubated with trypsin (1.5 mL/T75 flask, 5 mL/T175 flask) for 5 min under standard culture conditions. Cells were harvested by the addition of fully supplemented RPMI 1640 medium and subsequent transfer to a new T75 (2.5 mL of medium for cell collection) or T175 culture flask (7.5 mL of medium for cell collection) and further culturing. Cells were passaged at a 1:6 ratio. After reaching the desired number of cells, cells were harvested as described before and processed for bionanovesicles production as described in section 4.3.

4.2.2. Cell Culture for Cell-Based Assays

Cells, detached as described above, were collected into a sterile 50-mL polypropylene centrifuge tube and washed once (400 ×*g*, 5 min,

Table 1
Summary of liposomal and lipid-based ZnPC delivery systems for in vitro PDT studies.

Liposome composition	ZnPC:lipid molar ratio	Cell line	Tissue origin of cell line (species)	Light source and wavelength (nm)	Irradiance (W/cm^2)	Cumulative radiant exposure (J/cm^2)	NP concentrations investigated (**ZnPC** and lipid) (μM)	LC_{50} value (μM) (post-PDT measurement time)	Assay used	Ref.
TFK-1 cell-derived bionanovesicles (this study)	0.003	TFK-1	Extrahepatic cholangiocarcinoma (human)	Custom-made LED illumination device (650 ± 20 nm)	0.013	35.3	**0.15, 0.3, 0.75, 1.05, 1.5** 50, 100, 250, 350, 500	CVs: 1.11 (24 h), 0.70 (48 h), 0.55 (72 h) CMVs: 0.51 (24 h), 0.30 (48 h), 0.37 (72 h)	MTS	–
DPPC:cholesterol:DSPE-PEG (66:30:4)	0.003	SK-ChA-1	Extrahepatic cholangiocarcinoma (human)	Diode laser, 671 nm	0.263 (24-wells plate) 0.053 (6-wells plate)	15	**0, 0.15, 0.3, 0.6, 1.5** 0, 50, 100, 250, 500	0.75 (2 and 4 h)	WST-1	[7]
DPPC:DC-cholesterol: cholesterol:DSPE-PEG (66:25:5:4)	0.003	HUVECs	Human umbilical vein endothelial cells	Diode laser, 671 nm	0.263 (24-wells plate) 0.053 (6-wells plate)	15	**0, 0.03, 0.15** 0, 10, 50	0.03 (4 h)	WST-1	[11]
DPPC:DC-cholesterol: cholesterol:DSPE-PEG (66:25:5:4)	0.003	SK-ChA-1	Extrahepatic cholangiocarcinoma (human)	Diode laser, 671 nm	0.263 (24-wells plate) 0.053 (6-wells splate)	15	**0, 0.075, 0.24** 0, 25, 80	0.075 (4 h)	WST-1	[11]
DPPC:DC-cholesterol: cholesterol:DSPE-PEG (66:25:5:4)	0.003	A431	Epidermoid carcinoma (human)	Diode laser, 671 nm	0.263 (24-wells plate) 0.053 (6-wells plate)	15	**0, 0.195, 0.75** 0, 65, 250	0.195 (4 h)	WST-1	[11]
DPPC:DC-cholesterol: cholesterol:DSPE-PEG (66:25:5:4)	0.003	RAW 264.7	Monocyte/macrophage-like cells (murine)	Diode laser, 671 nm	0.263 (24-wells plate) 0.053 (6-wells plate)	15	**0, 0.09, 0.225** 0, 30, 75	0.09 (4 h)	WST-1	[11]
DPPC:DSPE-PEG (96:4)	0.003	A431	Epidermoid carcinoma (human)	Diode laser, 671 nm	0.263	15	**0.15, 0.3, 0.75, 1.05, 1.5** 50, 100, 250, 350, 500	0.82 (4 h), 0.37 (24 h) 0.51 (4 h), 0.13 (24 h)	WST-1 SRB	[19]
DPPC:DC-cholesterol: cholesterol:DSPE-PEG (66:25:5:4)	0.003	A431	Epidermoid carcinoma (human)	Diode laser, 671 nm	0.263	15	**0, 5, 10, 25** 0; 1667; 3333; 8333	10 (normoxic conditions), 5 (hypoxic conditions) (24 h)	WST-1	[10]
SPC:$C_{22}PEG_{900}GlcNAc$ (70:30); SPC consisted of DSPC (75%), DOPC (12%), and DPPC (8%)	0.0217 (*w/w*)	MDA-MB-231	Metastatic mammary adenocarcinoma (human)	Photon Laser, 675 nm	NR	8	**1.7, 3.4, 6.9, 13.8** 46, 92, 184, 369	~7 (24 h)	MTT	[118][1]
DPPC:DSPE-PEG (96:4)	0.003	SK-ChA-1	Extrahepatic cholangiocarcinoma (human)	Diode laser, 671 nm	0.263	15	**0.15, 0.3, 0.75, 1.05, 1.5** 50, 100, 250, 350, 500	WST-1: 0.22 (4 h), 0.25 (24 h) SRB: 1.14 (4 h), 0.16 (24 h)	WST-1, SRB	[12]
DPPC:DSPE-PEG (96:4)	0.003	HUVECs	Human umbilical vein endothelial cells	Diode laser, 671 nm	0.263	15	**0.15, 0.3, 0.75, 1.05, 1.5** 50, 100, 250, 350, 500	WST-1: 3.93 (4 h), 4.04 (24 h) SRB: 2.27 (4 h), 1.87 (24 h)	WST-1, SRB	[12]
DPPC:DSPE-PEG (96:4)	0.003	NIH-3T3	Embryonic fibroblast (murine)	Diode laser, 671 nm	0.263	15	**0.15, 0.3, 0.75, 1.05, 1.5** 50, 100, 250, 350, 500	WST-1: 5.72 (4 h), 0.60 (24 h) SRB: 3.17 (4 h), 2.03 (24 h)	WST-1, SRB	[12]

(*continued on next page*)

Table 1 (*continued*)

Liposome composition	ZnPC:lipid molar ratio	Cell line	Tissue origin of cell line (species)	Light source and wavelength (nm)	Irradiance (W/cm^2)	Cumulative radiant exposure (J/cm^2)	NP concentrations investigated (**ZnPC** and lipid) (μM)	LC_{50} value (μM) (post-PDT measurement time)	Assay used	Ref.
DPPC:DSPE-PEG (96:4)	0.003	RAW 264.7	Monocyte/macrophage-like cells (murine)	Diode laser, 671 nm	0.263	15	**0.15, 0.3, 0.75, 1.05, 1.5** 50, 100, 250, 350, 500	WST-1: 0.62 (4 h), 0.48 (24 h) SRB: 1.12 (4 h), 0.91 (24 h)	WST-1, SRB	[12]
SPC:DSPE-PEG (14:1 *w/w*)	0.13 (weight ratio)	HeLa	Cervical adenocarcinoma (human)	638 nm	NR	NR	**1.1, 2.2, 4.3, 8.7, 17.3** 8.5, 16.9, 33.8, 67.7, 135.4	2.3 (6 h)	MTT	[119] [2]
Lecithin:cholesterol (35:22)	0.018; lecithin: cholesterol: ZnPC*: 35:22:1	HepG2	Hepatocellular carcinoma (human)	> 610 nm	0.015	27	NR	0.16 (24 h)	MTT	[120] [3]
DMPC:DOTAP:DSPE-PEG_{2000} (78.3:20:0 and 74.5:20:3.8)	0.017	H460	Non-small cell lung cancer (human)	Laser, 660 nm	NR	NR (10 J cumulative energy)	**0, 0.4, 1.4, 5.2, 15.6**	~1.5 (78.3:20:0) and > 5.2 (74.5:20:3.8) (24 h)	MTT	[112]
DMPC:DOTAP:DSPE-PEG_{2000} (78.3:20:0 and 74.5:20:3.8)	0.017	CT26	Undifferentiated colon carcinoma (murine origin)	Laser, 660 nm	NR	NR (10 J cumulative energy)	**0, 0.4, 1.4, 5.2, 15.6**	16 (78.3:20:0) and > 16 (74.5:20:3.8) (24 h)	MTT	[112]
DMPC:DOTAP:DSPE-PEG_{2000} (78.3:20:0 and 74.5:20:3.8)	0.017	U-87 MG	Human glioblastoma (human)	Laser, 660 nm	NR	NR (10 J cumulative energy)	**0, 0.4, 1.4, 5.2, 15.6**	~5 (78.3:20:0) and 16 (74.5:20:3.8)	MTT	[112]
SPC:DSPE-PEG (14:1 *w/w*)	0.13 (weight ratio)	HeLa	Cervical adenocarcinoma (human)	630 nm	NR	NR	**1.1, 2.2, 4.3, 8.7, 17.3** 8.5, 16.9, 33.8, 67.7, 135.4	~2 (6 h)	MTT	[121] [4]
SPC:$C_{22}PEG_{900}$GlcNAc (70:30) SPC composition: 75% DSPC, 12% DOPC, 8% DPPC	21.7 (weight ratio)	MDA-MB-231	Metastatic mammary adenocarcinoma (human)	Photon Lase I system, 675 nm	NR	8	**1.7, 3.5, 6.9, 13.8** 46, 92, 184, 369	6.9 (24 h)	MTT	[122] [5]

Abbreviations: NP, nanoparticle, ZnPC; zinc phthalocyanine; ZnPC*, monosubstituted ZnPC (ZnPC-S$(CH_2)_3SO_3$ and ZnPC-O$(CH_2)_3SO_3$); SRB, sulforhodamine B; CV, cell-derived vesicle; CMV, cell membrane-derived vesicle; WST-1, water-soluble tetrazolium salt (mitochondrial redox); NR, not reported; DPPC, 1,2-dipalmitoyl-*sn*-glycero-3-phosphocholine; DSPE-PEG,distearoylphosphatidylethanolamine-poly(ethylene glycol); DOPC, dioleoylphosphatidylcholine; MTT, 3-(4,5-dimethylthiazol-2-yl)-2,5-diphenyltetrazolium bromide; SPC, soybean phosphatidylcholine; MTS, 3-(4,5-dimethylthiazol-2-yl)-5-(3-carboxymethoxyphenyl)-2-(4-sulfophenyl)-2H-tetrazolium; $C_{22}PEG_{900}$GlcNAc, glycosylated polymeric amphiphile *N*-acetyl-β-d-glucosaminyl-PEG900-docosanate conjugate; DSPC, 1,2-distearoyl-*sn*-glycero-3-phosphocholine; DMPC, 1,2-dimyristoyl-*sn*-glycero-3-phosphocholine; DOTAP, 1,2-dioleoyl-3-trimethylammonium-propane.

Notes: [1] Liposomes co-encapsulated diethyldithiocarbamate, a chelating agent (clinically used for the treatment of acute nickel carbonyl poisoning); [2] ZnPC-phospholipid complex co-encapsulated methotrexate for PDT + chemotherapy; [3] authors synthesized zinc (II) phthalocyanines monosubstituted with a sulphonate group in the alpha position with "O bridge" and "S bridge" as bonds; [4] ZnPC-phospholipid complex co-encapsulated doxorubicin for PDT + chemotherapy; [5] phospholipid complex self-assembled nanoparticles with surface-grafted methotrexate-DSPE-PEG.

RT) and resuspended in fresh, fully supplemented RPMI 1640 medium. Cells were counted using a hemocytometer (aliquot of 10 µL). Next, cells were seeded into 48-wells plates (flow cytometry) or 96-wells plates (confocal microscopy, dark toxicity, PDT efficacy) 24 h prior to an experiment unless stated otherwise. A seeding density of 3.5×10^4 cells/well (48-wells plates, 200 µL/well) and 1.5×10^4 cells/well (96-wells plates, 100 µL/well), yielding a confluence of 60–70%, was used to achieve ~90% confluence at the time of the experiment. During the experiments, RPMI 1640 medium without FBS, additional L-glutamine, and phenol red but with antibiotics (final concentration of 100 U/mL penicillin, 100 µg/mL streptomycin), referred to as $RPMI^{-/-}$, was used when cells were incubated with PS.

4.3. Preparation and Characterization of Bionanovesicles

TFK-1 cells were cultured and harvested as described in section 4.2.1. After harvesting, cells derived from four T175 flasks were pooled in two 50-mL polypropylene centrifuge tubes and washed twice (centrifugation at 300 ×*g*, 5 min, RT) with 20 mL of 0.22-µm filter-sterilized physiological saline. Cell pellets were gently resuspended in 10 mL of 10 mM HEPES buffer, pH = 7.5 (for CV preparation; section 4.3.1), or fractionation medium (for CMV preparation; section 4.3.2) and processed as illustrated in Fig. 7.

4.3.1. Preparation of Cellular Vesicles (CVs)

Cells from two T175 flasks were suspended in 10 mL of 10 mM HEPES buffer, pH = 7.5, and sonicated with a 12.8-mm tip at 10% power (40 W) for 2 min (10 s on and 10 s off) on ice and filtered once through a 0.2-µm polyethersulfone (PES) membrane filter. The CVs were stored in sterile 15-mL or 50-mL polypropylene centrifuge tubes at 4 °C in the dark under a nitrogen atmosphere for a maximum of 1 wk. Dilutions of the stock were performed with 10 mM HEPES buffer, pH = 7.5.

4.3.2. Preparation of Cell Membrane Vesicles (CMVs)

Cells from two T175 flasks were suspended with 10 mL fractionation medium (0.25 M sucrose, 1 mM EDTA, 20 mM HEPES, and protease inhibitor cocktail (pH = 7.4) [114,115]) and incubated on ice for 1 h. The cell suspension was sonicated using a tip sonicator for 30 rounds on ice (t_{on} = 3 s, t_{off} = 7 s) at 10% power (40 W). The solution was centrifuged at 3000 ×*g* for 10 min at 4 °C and the supernatant was collected and centrifuged at 13,500 ×*g* for 20 min at 4 °C. The pellets were washed twice with 10 mM HEPES solution, pH = 7.5 (13,500 ×g, 20 min, 4 °C) and resuspended in 10 mL MilliQ water. The cell membrane mixture was bath-sonicated under ice-cold conditions (to avoid thermal denaturation of protein) for 15 min until the mixture solution became semi-opaque. Finally, the suspension was filtered once through a 0.2-µm PES membrane filter. The CMVs were stored in sterile 15-mL or

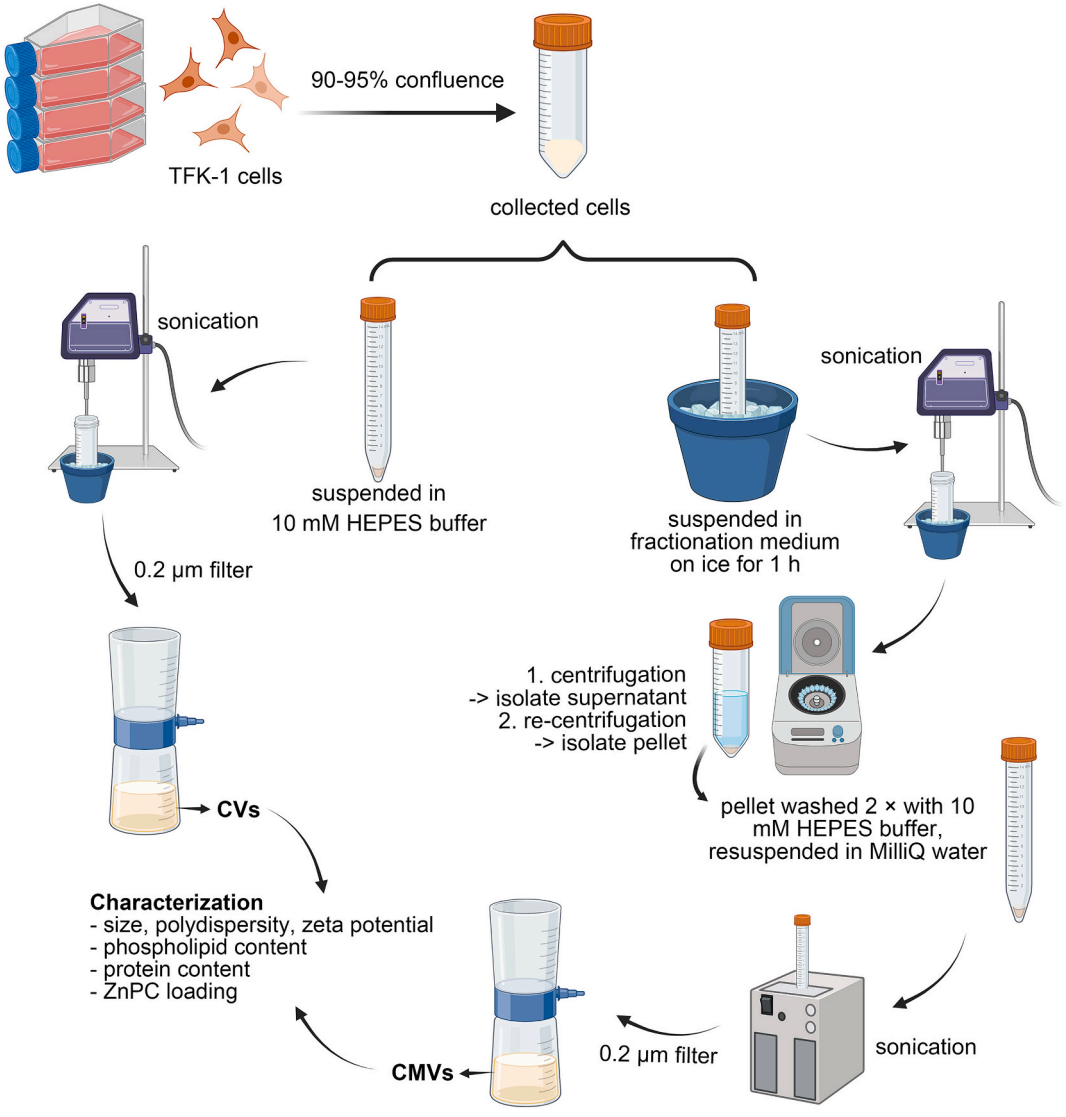

Fig. 7. Schematic overview of the cellular vesicle (CV) and cell membrane vesicle (CMV) preparation method.

50-mL polypropylene centrifuge tubes at 4 °C in the dark under a nitrogen atmosphere for a maximum of 1 wk. Dilutions of the stock were done with MilliQ water.

4.3.3. Characterization of CVs and CMVs

Phospholipid concentration of CVs and CMVs derived from 4 T175 flasks according to Fig. 7 was determined by a modified inorganic phosphate assay [116] developed by Rouser et al. [117]. An aliquot (10 μL) of CVs or CMVs ($N = 3$ per sample) was transferred into a 10-mL round-bottom borosilicate glass tube. Simultaneously, aliquots of inorganic phosphate standard were loaded into a glass tube (10 mM sodium dihydrogen phosphate stock solution; NaH_2PO_4 in MilliQ water) in the 0–100 nmol range. Samples were desiccated in a heating block (180 °C) for 30 min and allowed to cool down at RT. Next, 300 μL of 70% $HClO_4$ was deposited into each tube using a bottle-top dispenser and tubes were topped off with pre-washed and dried glass marbles. The samples were digested in a heating block (180 °C) for at least 1 h and at most 3 h. Following cooling at RT, 1 mL of MilliQ water, 500 μL of 1.2% *w/v* ammonium molybdate, and 500 μL of freshly prepared 5% w/v ascorbic acid were sequentially added to each tube with intermittent vortexing of the mixtures. Finally, the samples were placed in boiling water for 5 min, allowed to cool at RT, and transferred (100 μL) to a 96-well plate. Absorbance was measured at 797 nm using a plate reader and the sample concentration was calculated by solving the linear fit equation of the standard curve.

CV and CMV size and polydispersity index (PDI) were determined by photon correlation spectroscopy (Zetasizer Nano, Malvern Instruments, Malvern, UK) from 10 × 10 measurements per sample using the following settings: unimodal analysis, refractive index (RI) dispersant = 1.331, viscosity = 0.8872, temperature = 25 °C, scattering angle = 175°, measure position at 4.65 mm from the cell wall, diffusion coefficient = 1.61. The zeta potential, which is a rough indication of the surface charge of the particle, was measured using electrophoretic light scattering (Zetasizer Nano, Malvern Instruments). The zeta potential of CVs and CMVs was corrected for the zeta potential of the equilibration buffer.

The morphology of CVs and CMVs was determined by transmission electron microscopy (TEM). Ten μL of sample was applied to a 300-mesh copper grid coated with formvar and carbon and allowed to interact for 2 min. Excess liquid was absorbed using ashless filter paper positioned at the grid's periphery. Subsequently, 5 μL of a 2% (*w/v*) uranyl acetate staining solution (pH = 4.5) was immediately added to the grid, followed by a 1-min incubation period. Excess staining solution was carefully removed and the grid was left to air-dry. The prepared samples were examined using TEM on a Tecnai 20 TOMO instrument (FEI Company, Hillsboro, OR, USA).

4.3.4. Preparation and Characterization of ZnPC-CVs and ZnPC-CMVs

CVs and CMVs were prepared as described in sections 4.3.1 and 4.3.2, respectively, and characterized for phospholipid content as described in section 4.3.3. ZnPC in pyridine was added to the bionanovesicle suspension at the desired PS:phospholipid ratio. ZnPC was diluted with pyridine where applicable, whereas the bionanovesicles were diluted in the respective carrier solutions (sections 4.3.1 and 4.3.2).

For the loading efficiency, physicochemical characterization, and absorption spectroscopy experiments, 5–100 μM of ZnPC in 50 μL of pyridine was added to CVs and CMVs at a fixed phospholipid concentration (500 μM final phospholipid concentration (section 4.3.3), 0.45 mL volume), accounting for a ZnPC:phospholipid ratio of 0.001–0.02. The pyridine concentration was kept constant at 10% (*v/v*). To prepare bionanovesicles at a 0.03 ZnPC:phospholipid molar ratio (15 μM of ZnPC), 75 μL of 100 μM ZnPC in pyridine was added to 425 μL of CV/CMV suspension, accounting for a final phospholipid concentration of 500 μM and a 15% (v/v) pyridine concentration. In a separate absorption spectroscopy experiment, where the phospholipid content was increased while holding the PS concentration constant, bionanovesicles containing 0.5 μM ZnPC were prepared by adding 50 μL of 5 μM ZnPC in pyridine to 450 μL of CVs/CMVs at varying phospholipid concentrations.

For fluorescence spectroscopy experiments, bionanovesicles containing 1.5 μM ZnPC were prepared by adding 50 μL of 15 μM ZnPC in pyridine to 450 μL CVs/CMVs (500 μM phospholipid concentration), accounting for a ZnPC:phospholipid molar ratio of 0.003.

The mixtures were sonicated using a sonic dismembrator (Qsonica, Newtown, CT, USA) with a 1/16-in. (1.6-mm) tip at the following settings: 25% amplitude and 3 cycles of 10 s on/off for 1 min with a 2-min cooling period between each cycle. The PS-containing bionanovesicles were subsequently incubated on a roller for 2 h at RT. ZnPC-CVs and ZnPC-CMVs were stored at 4 °C under a nitrogen atmosphere in the dark for up to 1 wk. We have demonstrated previously that biomembrane-embedded ZnPC remains stable and intact under these conditions for up to 8 wk [10].

Determination of diameter and PDI was performed as described in section 2.3.3. Since ZnPC has no expected effect on biomembrane surface charge due to its inner membrane localization, zeta potential measurements were omitted for ZnPC-CVs and ZnPC-CMVs.

The amount of ZnPC intercalated into the bionanovesicle membrane was determined by Bland-Altman analysis [86] using absorption spectroscopy. CVs and CMVs were loaded with ZnPC at a PS:phospholipid ratio of 0.001, 0.002, 0.003, 0.004, 0.005, 0.006, 0.007, 0.008, 0.009, 0.01, 0.02, and 0.03 as described above. A 40-μL aliquot of ZnPC-CVs in 10 mM HEPES buffer, pH = 7.5, or ZnPC-CMVs in MilliQ was transferred into an Eppendorf tube containing 360 μL of pyridine ($N = 3$/ZnPC: phospholipid ratio), briefly bath-sonicated, and centrifuged at 1000 ×*g* for 5 min at RT. Eppendorf tubes are composed of polypropylene, which has excellent chemical compatibility with pyridine [https://www.dutscher.com/data/pdf_guides/en/CCTPPA.pdf, accessed 11 December 2023]. ZnPC standards were prepared in 10 mM HEPES, pH = 7.5/pyridine (CVs) and MilliQ water/pyridine (CMVs) at the same volume ratios (1:9, respectively) in a 0.1–0.8 μM ZnPC concentration range and a 100-μL aliquot was transferred to a medical grade polystyrene clear bottom black 96-wells microplate. Polystyrene and pyridine also have excellent chemical compatibility [https://www.dutscher.com/data/pdf_guides/en/CCTPPA.pdf, accessed 11 December 2023]. Finally, 100 μL of the sample supernatant was transferred to the microplate and the absorbance was read in a microplate reader at 674 nm [7]. Analyte concentrations were calculated from the linear fit function of the standard curve, averaged, and presented in Bland-Altman plots (GraphPad Prism) as the nominal concentration difference (in μM) between (measured ZnPC- added ZnPC). This method measures actual intramembrane ZnPC content and does not suffer from quantum chemical effects associated with ZnPC dimer-/multimerization in biomembranes at higher PS:phospholipid ratios [7,87].

4.4. Spectral Properties of ZnPC-CVs and ZnPC-CMVs

The ZnPC-CVs and ZnPC-CMVs used were prepared as described in section 4.3.4. The absorption spectra of ZnPC in pyridine (1.5 μM) and ZnPC-CVs and ZnPC-CMVs (ZnPC:phospholipid molar ratio of 0.003) in their respective carrier solutions (sections 4.3.1 and 4.3.2) were acquired with a UV 2450 spectrophotometer (Shimadzu, Kyoto, Japan) at a scan rate of 100 nm/min. Before spectral acquisition the samples were blanked with 10 mM HEPES solution, pH = 7.5 (CVs) and MilliQ water (CMVs).

ZnPC, ZnPC-CVs, and ZnPC-CMVs fluorescence emission and excitation spectra were measured with a spectrofluorometer (model FP-8300, Jasco, Tokyo, Japan) at $\lambda_{ex} = 650 \pm 5$ nm and $\lambda_{em} = 695 \pm 5$ nm, respectively. Gain was set at 390 V and the scan rate was 100 nm/min. Fluorescence emission and excitation spectra were background-corrected and normalized to maximum value.

4.5. Analysis of Bionanovesicle-Tumor Cell Interactions

4.5.1. ZnPC-CV and ZnPC-CMV Association with Tumor Cells (Flow Cytometry)

The interaction between PSs and TFK-1 cells was studied by flow cytometry. Cells were seeded in 48 wells plates at a density of 3.5×10^4 cells/well (200 μL/well) and incubated overnight. Cells were subsequently incubated with PSs (200 μL/well) in RPMI$^{-/-}$ for 1-, 30-, 60-, and 120 min at standard culture conditions. The final PS concentration was 0.3 μM for free ZnPC, ZnPC-CVs and ZnPC-CMVs (ZnPC:phospholipid molar ratio of 0.003). Two hundred μL of PSs at different ZnPC: phospholipid molar ratios (0.001, 0.009, 0.03) and 500-μM lipid concentration (CVs/CMVs) were also used to assay association with cells as described above. After harvesting with 100 μL of accutase for 10 min at standard culture conditions, cells were collected and transferred from each well to 96 well plates, and the samples were analyzed by flow cytometry. Viable cells were gated based on their preset forward-scatter and side-scatter properties. PS autofluorescence was measured at $\lambda_{ex} = 633$ nm and $\lambda_{em} = 661 \pm 20$ nm and a fixed detector voltage (625 V). The excitation wavelength coincides with the blue Q-band absorption shoulder of the photosensitizers and causes autofluorescence as a result of radiative S1 → S0 state decay of a small fraction of the excited state electrons. Ten thousand events were collected in the gated region. Association was calculated from the difference between the mean fluorescence intensity of photosensitized cells relative to the mean fluorescence intensity of non-photosensitized cells ($N = 3$ independent experiments per incubation time). Data were processed in FlowJo software (BD Biosciences, Franklin Lakes, NJ, USA).

4.5.2. ZnPC-CV and ZnPC-CMV Uptake and Intracellular Distribution in Tumor Cells (Confocal Microscopy)

ZnPC uptake was assessed by confocal laser scanning microscopy with a Yokogawa High Content Imaging Platform (model CV7000S, Yokogawa, Tokyo, Japan) using a 40 × objective. TFK-1 cells (100 μL) were seeded in 96 wells plates (flat bottom clear, black polypropylene) at a density of 1.5×10^4 cells per well. The cells were incubated overnight until 60–70% confluence. Upon reaching the target confluence, cells were incubated with the ZnPC (100 μL/well) in RPMI$^{-/-}$ for 15 min, 30 min, and 60 min at standard culture conditions. The final PS concentrations were 3 μM for free ZnPC, ZnPC-CVs, and ZnPC-CMVs. Next, cells were washed with PBS (RT, 100 μL/well) prior to fixation with 2% paraformaldehyde (PFA, 100 μL/well) in PBS (RT) for 15 min in the dark. The fixative solution was decanted and wells were washed once with PBS (RT) and submersed in 100 μL of ice-cold PBS for storage at 4 °C until confocal microscopy imaging (typically within 24 h). Directly before imaging, 100 μL of diluted Hoechst 33342 (10 μg/mL in PBS) was added to each sample and incubated for 3 min at RT to stain nuclear DNA. Next, Hoechst 33342 was decanted, wells were washed twice with PBS (RT), and 100 μL of PBS (RT) was added to each well. Imaging was performed at the following settings: Hoechst, $\lambda_{ex} = 405$ nm, $\lambda_{em} = 479$ nm; ZnPC-CVs and ZnPC-CMVs, $\lambda_{ex} = 660$ nm, $\lambda_{em} = 790$ nm.

4.6. Dark Toxicity

The dark toxicity of ZnPC-CVs and ZnPC-CMVs was assessed in TFK-1 cells in the absence of illumination. Cells seeded in 96-wells plates were cultured as described in section 4.2.2. The cells were incubated overnight until ~90% confluence. Upon reaching the target confluence, cells were washed with PBS at RT, and PS in RPMI$^{-/-}$ was added at concentrations ranging from 0 to 1.5 μM for free ZnPC, ZnPC-CVs, and ZnPC-CMVs (0–500 μM phospholipid concentration). Medium containing 1% Triton X-100 was used as positive control for complete cell death and RPMI$^{-/-}$ as negative control. After 24-h, 48-h, and 72-h incubation with the ZnPC at standard culture conditions, the MTS assay was performed according to the manufacturer's instructions. In short, 20 μL/well of CellTiter 96 Aqueous One Solution (Promega) was added and plates were incubated at standard culture conditions for 1 h. Cell viability was determined by measuring absorbance at 490 nm with GloMax Discover Microplate Reader (Promega) and reported as percentage viability relative to negative control cells.

4.7. Photodynamic Therapy

For PDT efficacy experiments, TFK-1 cells were cultured and seeded in 96-wells plates as described in section 4.2.1 and 4.2.2. The cells were incubated overnight until 90% confluence. Upon reaching the target confluence, cells were washed with PBS (RT). In a first test arm, PS (free ZnPC, ZnPC-CVs, or ZnPC-CMVs) in RPMI$^{-/-}$ was added at concentrations ranging from 0 to 1.5 μM at a fixed 0.003 ZnPC:phospholipid ratio. In a second test arm, ZnPC-CVs and ZnPC-CMVs were added to cells at increasing ZnPC:phospholipid ratios and fixed phospholipid concentration (100 μM; 5 μL of CVs/CMVs in 95 μL medium per well). Medium containing 1% Triton X-100 was used as positive control for complete cell death and RPMI$^{-/-}$ medium was used as negative control. Empty CVs and CMVs were employed for the 0 μM ZnPC group. Cells were incubated with bionanovesicles for 1 h under standard culture conditions and washed twice with RPMI$^{-/-}$ and once with PBS (RT). Next, 100 μL of fresh RPMI$^{-/-}$ (37 °C) was added to each well and cells were illuminated with a custom-made LED device (1 LED per well, $\lambda = 650 \pm 20$ nm) at 5 mW for 40 min (the beam diameter was comparable to the well diameter; i.e., 6.58 mm inner diameter), equating to a total incident energy of 12 J/well and a cumulative radiant exposure of 35.3 J/cm^2. The radiant exposure was measured with an optometer. Cell viability assays were performed at 24 h, 48 h, and 72 h after PDT using the MTS assay. Data points were fitted in GraphPad Prism using nonlinear regression curve fitting (inhibitor vs. normalized response – variable slope) to derive LC_{50} values.

Funding

This research was funded by grants from the Dutch Cancer Foundation (KWF project # 10666), a Zhejiang Provincial Foreign Expert Program Grant, Zhejiang Provincial Key Natural Science Foundation of China (#Z20H160031), a Basic Public Welfare Research Project of Zhejiang Province (LGD21H300001), and a Science and Technology Planning Project of Jiaxing City, Zhejiang Province (2019AY32012). WP was sponsored by a grant from the National Natural Science Foundation of China (31871402). HS received financial support from the National Natural Science Foundation of China. YSK was supported by the Academy of Medical Sciences (SGL027/1011). ML was supported by a Chinese Scholarship Council grant (202108330069).

CRediT authorship contribution statement

Mingjuan Li: Writing – review & editing, Writing – original draft, Visualization, Methodology, Investigation, Funding acquisition, Formal analysis, Data curation, Conceptualization. **Esmeralda D.C. Bosman:** Writing – review & editing, Methodology, Investigation, Formal analysis, Data curation. **Olivia M. Smith:** Writing – review & editing, Investigation, Formal analysis, Data curation. **Nicole Lintern:** Writing – review & editing, Investigation, Formal analysis, Data curation. **Daniel J. de Klerk:** Writing – review & editing, Validation, Formal analysis. **Hong Sun:** Writing – review & editing, Supervision, Formal analysis. **Shuqun Cheng:** Writing – review & editing, Supervision, Resources, Funding acquisition. **Weiwei Pan:** Writing – review & editing, Supervision, Resources, Funding acquisition. **Gert Storm:** Writing – review & editing, Supervision, Resources. **Yazan S. Khaled:** Writing – review & editing, Supervision, Resources, Funding acquisition. **Michal Heger:** Writing – review & editing, Writing – original draft, Visualization, Supervision, Software, Resources, Project administration, Methodology, Funding acquisition, Formal analysis, Data curation, Conceptualization.

Declaration of generative AI and AI-assisted technologies in the writing process

No AI or AI tools were used in any aspect of this manuscript.

Declaration of competing interest

The authors declare the following financial interests/personal relationships which may be considered as potential competing interests:

Michal Heger reports financial support was provided by Dutch Cancer Society. Michal Heger reports financial support was provided by Zhejiang Provincial Key Natural Science Foundation of China. Michal Heger reports financial support was provided by Basic Public Welfare Research Project of Zhejiang Province. Mingjuan Li reports financial support was provided by Science and Technology Planning Project of Jiaxing City, Zhejiang Province. Weiwei Pan reports financial support was provided by National Natural Science Foundation of China. Yazan S. Khaled reports financial support was provided by Academy of Medical Sciences. Mingjuan Li reports financial support was provided by Chinese Scholarship Council. If there are other authors, they declare that they have no known competing financial interests or personal relationships that could have appeared to influence the work reported in this paper.

Data availability

Data will be made available on request.

Acknowledgments

ML, GS, and MH are thankful to Bárbara Mesquita, Kim van der Wurff-Jacobs, Boning Qiu, and Roel Maas-Bakker for their assistance with some of the experiments.

Appendix A. Supplementary data

Supplementary data to this article can be found online at https://doi.org/10.1016/j.jphotobiol.2024.112903.

References

[1] F.S. Hodi, S.J. O'Day, D.F. McDermott, R.W. Weber, J.A. Sosman, J.B. Haanen, R. Gonzalez, C. Robert, D. Schadendorf, J.C. Hassel, et al., Improved survival with ipilimumab in patients with metastatic melanoma, N. Engl. J. Med. 363 (2010) 711–723, https://doi.org/10.1056/NEJMoa1003466.

[2] P. Schmid, S. Adams, H.S. Rugo, A. Schneeweiss, C.H. Barrios, H. Iwata, V. Dieras, R. Hegg, S.A. Im, G. Shaw Wright, et al., Atezolizumab and nab-paclitaxel in advanced triple-negative breast cancer, N. Engl. J. Med. 379 (2018) 2108–2121, https://doi.org/10.1056/NEJMoa1809615.

[3] P.M. Forde, J.E. Chaft, D.M. Pardoll, Neoadjuvant PD-1 blockade in resectable lung cancer, N. Engl. J. Med. 379 (2018) e14, https://doi.org/10.1056/NEJMc1808251.

[4] A. Ribas, Releasing the brakes on cancer immunotherapy, N. Engl. J. Med. 373 (2015) 1490–1492, https://doi.org/10.1056/NEJMp1510079.

[5] R.J. Motzer, B. Escudier, D.F. McDermott, S. George, H.J. Hammers, S. Srinivas, S.S. Tykodi, J.A. Sosman, G. Procopio, E.R. Plimack, et al., Nivolumab versus Everolimus in advanced renal-cell carcinoma, N. Engl. J. Med. 373 (2015) 1803–1813, https://doi.org/10.1056/NEJMoa1510665.

[6] W. Jiang, M. Liang, Q. Lei, G. Li, S. Wu, The current status of photodynamic therapy in Cancer treatment, Cancers (Basel) 15 (2023), https://doi.org/10.3390/cancers15030585.

[7] M. Broekgaarden, A.I. de Kroon, T.M. Gulik, M. Heger, Development and in vitro proof-of-concept of interstitially targeted zinc- phthalocyanine liposomes for photodynamic therapy, Curr. Med. Chem. 21 (2014) 377–391, https://doi.org/10.2174/09298673113209990211.

[8] R. Weijer, M. Broekgaarden, M. Krekorian, L.K. Alles, A.C. van Wijk, C. Mackaaij, J. Verheij, A.C. van der Wal, T.M. van Gulik, G. Storm, et al., Inhibition of hypoxia inducible factor 1 and topoisomerase with acriflavine sensitizes perihilar cholangiocarcinomas to photodynamic therapy, Oncotarget 7 (2016) 3341–3356, https://doi.org/10.18632/oncotarget.6490.

[9] R. Weijer, M. Broekgaarden, R.F. van Golen, E. Bulle, E. Nieuwenhuis, A. Jongejan, P.D. Moerland, A.H. van Kampen, T.M. van Gulik, M. Heger, Low-power photodynamic therapy induces survival signaling in perihilar cholangiocarcinoma cells, BMC Cancer 15 (2015) 1014, https://doi.org/10.1186/s12885-015-1994-2.

[10] M. Broekgaarden, R. Weijer, M. Krekorian, B. van den Ijssel, M. Kos, L.K. Alles, A. C. van Wijk, Z. Bikadi, E. Hazai, T.M. van Gulik, et al., Inhibition of hypoxia-inducible factor 1 with acriflavine sensitizes hypoxic tumor cells to photodynamic therapy with zinc phthalocyanine-encapsulating cationic liposomes, Nano Res. 9 (2016) 1639–1662, https://doi.org/10.1007/s12274-016-1059-0.

[11] R. Weijer, S. Clavier, E.A. Zaal, M.M. Pijls, R.T. van Kooten, K. Vermaas, R. Leen, A. Jongejan, P.D. Moerland, A.H. van Kampen, et al., Multi-OMIC profiling of survival and metabolic signaling networks in cells subjected to photodynamic therapy, Cell. Mol. Life Sci. 74 (2017) 1133–1151, https://doi.org/10.1007/s00018-016-2401-0.

[12] L.M. Dias, M.J. de Keijzer, D. Ernst, F. Sharifi, D.J. de Klerk, T.G. Kleijn, E. Desclos, J.A. Kochan, L.R. de Haan, L.P. Franchi, et al., Metallated phthalocyanines and their hydrophilic derivatives for multi-targeted oncological photodynamic therapy, J. Photochem. Photobiol. B 234 (2022) 112500, https://doi.org/10.1016/j.jphotobiol.2022.112500.

[13] J.M. Banales, V. Cardinale, G. Carpino, M. Marzioni, J.B. Andersen, P. Invernizzi, G.E. Lind, T. Folseraas, S.J. Forbes, L. Fouassier, et al., Expert consensus document: cholangiocarcinoma: current knowledge and future perspectives consensus statement from the European network for the study of cholangiocarcinoma (ENS-CCA), Nat. Rev. Gastroenterol. Hepatol. 13 (2016) 261–280, https://doi.org/10.1038/nrgastro.2016.51.

[14] C.S. Shim, Y.K. Cheon, S.W. Cha, S. Bhandari, J.H. Moon, Y.D. Cho, Y.S. Kim, L. S. Lee, M.S. Lee, B.S. Kim, Prospective study of the effectiveness of percutaneous transhepatic photodynamic therapy for advanced bile duct cancer and the role of intraductal ultrasonography in response assessment, Endoscopy 37 (2005) 425–433, https://doi.org/10.1055/s-2005-861294.

[15] T. Zoepf, R. Jakobs, J.C. Arnold, D. Apel, J.F. Riemann, Palliation of nonresectable bile duct cancer: improved survival after photodynamic therapy, Am. J. Gastroenterol. 100 (2005) 2426–2430, https://doi.org/10.1111/j.1572-0241.2005.00318.x.

[16] M. Wiedmann, F. Berr, I. Schiefke, H. Witzigmann, K. Kohlhaw, J. Mossner, K. Caca, Photodynamic therapy in patients with non-resectable hilar cholangiocarcinoma: 5-year follow-up of a prospective phase II study, Gastrointest. Endosc. 60 (2004) 68–75, https://doi.org/10.1016/s0016-5107(04)01288-x.

[17] M.E. Ortner, K. Caca, F. Berr, J. Liebetruth, U. Mansmann, D. Huster, W. Voderholzer, G. Schachschal, J. Mossner, H. Lochs, Successful photodynamic therapy for nonresectable cholangiocarcinoma: a randomized prospective study, Gastroenterology 125 (2003) 1355–1363, https://doi.org/10.1016/j.gastro.2003.07.015.

[18] F.L. Dumoulin, T. Gerhardt, S. Fuchs, C. Scheurlen, M. Neubrand, G. Layer, T. Sauerbruch, Phase II study of photodynamic therapy and metal stent as palliative treatment for nonresectable hilar cholangiocarcinoma, Gastrointest. Endosc. 57 (2003) 860–867, https://doi.org/10.1016/s0016-5107(03)70021-2.

[19] L.M. Dias, F. Sharifi, M.J. de Keijzer, B. Mesquita, E. Desclos, J.A. Kochan, D.J. de Klerk, D. Ernst, L.R. de Haan, L.P. Franchi, et al., Attritional evaluation of lipophilic and hydrophilic metallated phthalocyanines for oncological photodynamic therapy, J. Photochem. Photobiol. B 216 (2021) 112146, https://doi.org/10.1016/j.jphotobiol.2021.112146.

[20] R. Weijer, M. Broekgaarden, M. Kos, R. van Vught, E.A. Rauws, E.J. Breukink, T. M. van Gulik, G. Storm, M. Heger, Enhancing photodynamic therapy of refractory solid cancers: combining second-generation photosensitizers with multi-targeted liposomal delivery, J. Photochem. Photobiol. C 23 (2015) 103–131, https://doi.org/10.1016/j.jphotochemrev.2015.05.002.

[21] D.J. de Klerk, M.J. de Keijzer, L.M. Dias, J. Heemskerk, L.R. de Haan, T.G. Kleijn, L.P. Franchi, M. Heger, Photodynamic Therapy Study, G, Strategies for improving photodynamic therapy through pharmacological modulation of the immediate early stress response, Methods Mol. Biol. 2451 (2022) 405–480, https://doi.org/10.1007/978-1-0716-2099-1_20.

[22] M. Broekgaarden, R. Weijer, T.M. van Gulik, M.R. Hamblin, M. Heger, Tumor cell survival pathways activated by photodynamic therapy: a molecular basis for pharmacological inhibition strategies, Cancer Metastasis Rev. 34 (2015) 643–690, https://doi.org/10.1007/s10555-015-9588-7.

[23] M.J. de Keijzer, D.J. de Klerk, L.R. de Haan, R.T. van Kooten, L.P. Franchi, L. M. Dias, T.G. Kleijn, D.J. van Doorn, M. Heger, Photodynamic Therapy Study, G, Inhibition of the HIF-1 survival pathway as a strategy to augment photodynamic therapy efficacy, Methods Mol. Biol. 2451 (2022) 285–403, https://doi.org/10.1007/978-1-0716-2099-1_19.

[24] S.L. Jacques, How tissue optics affect dosimetry of photodynamic therapy, J. Biomed. Opt. 15 (2010) 051608, https://doi.org/10.1117/1.3494561.

[25] R. Lindberg-Larsen, H. Solvsten, K. Kragballe, Evaluation of recurrence after photodynamic therapy with topical methylaminolaevulinate for 157 basal cell carcinomas in 90 patients, Acta Derm. Venereol. 92 (2012) 144–147, https://doi.org/10.2340/00015555-1198.

[26] A. Casas, G. Di Venosa, T. Hasan, B. Al, Mechanisms of resistance to photodynamic therapy, Curr. Med. Chem. 18 (2011) 2486–2515, https://doi.org/10.2174/092986711795843272.

[27] C.E. Olsen, A. Weyergang, V.T. Edwards, K. Berg, A. Brech, S. Weisheit, A. Hogset, P.K. Selbo, Development of resistance to photodynamic therapy (PDT) in human breast cancer cells is photosensitizer-dependent: possible mechanisms and approaches for overcoming PDT-resistance, Biochem. Pharmacol. 144 (2017) 63–77, https://doi.org/10.1016/j.bcp.2017.08.002.

[28] J. Lou, M. Aragaki, N. Bernards, T. Chee, A. Gregor, Y. Hiraishi, T. Ishiwata, C. Leung, L. Ding, S. Kitazawa, et al., Repeated photodynamic therapy mediates the abscopal effect through multiple innate and adaptive immune responses with

and without immune checkpoint therapy, Biomaterials 292 (2023) 121918, https://doi.org/10.1016/j.biomaterials.2022.121918.
[29] R. Alzeibak, T.A. Mishchenko, N.Y. Shilyagina, I.V. Balalaeva, M.V. Vedunova, D. V. Krysko, Targeting immunogenic cancer cell death by photodynamic therapy: past, present and future, J. Immunother. Cancer 9 (2021), https://doi.org/10.1136/jitc-2020-001926.
[30] M. Broekgaarden, R. Weijer, A.C. van Wijk, R.C. Cox, M.R. Egmond, R. Hoebe, T. M. van Gulik, M. Heger, Photodynamic therapy with liposomal zinc phthalocyanine and tirapazamine increases tumor cell death via DNA damage, J. Biomed. Nanotechnol. 13 (2017) 204–220, https://doi.org/10.1166/jbn.2017.2327.
[31] M. Broekgaarden, M. Kos, F.A. Jurg, A.A. van Beek, T.M. van Gulik, M. Heger, Inhibition of NF-kappaB in tumor cells exacerbates immune cell activation following photodynamic therapy, Int. J. Mol. Sci. 16 (2015) 19960–19977, https://doi.org/10.3390/ijms160819960.
[32] M. Broekgaarden, R. van Vught, S. Oliveira, R.C. Roovers, P.M. van Bergen Henegouwen, R.J. Pieters, T.M. Van Gulik, E. Breukink, M. Heger, Site-specific conjugation of single domain antibodies to liposomes enhances photosensitizer uptake and photodynamic therapy efficacy, Nanoscale 8 (2016) 6490–6494, https://doi.org/10.1039/c6nr00014b.
[33] J. Zhu, S. Tian, K.T. Li, Q. Chen, Y. Jiang, H.D. Lin, L.H. Yu, D.Q. Bai, Inhibition of breast cancer cell growth by methyl pyropheophenylchlorin photodynamic therapy is mediated though endoplasmic reticulum stress-induced autophagy in vitro and vivo, Cancer Med. 7 (2018) 1908–1920, https://doi.org/10.1002/cam4.1418.
[34] X. Weng, D. Wei, Z. Yang, W. Pang, K. Pang, B. Gu, X. Wei, Photodynamic therapy reduces metastasis of breast cancer by minimizing circulating tumor cells, Biomed. Opt. Express 12 (2021) 3878–3886, https://doi.org/10.1364/BOE.429947.
[35] T.A. Theodossiou, M. Ali, M. Grigalavicius, B. Grallert, P. Dillard, K.O. Schink, C. E. Olsen, S. Walchli, E.M. Inderberg, A. Kubin, et al., Simultaneous defeat of MCF7 and MDA-MB-231 resistances by a hypericin PDT-tamoxifen hybrid therapy, NPJ Breast Cancer 5 (2019) 13, https://doi.org/10.1038/s41523-019-0108-8.
[36] J. Szebeni, F. Muggia, A. Gabizon, Y. Barenholz, Activation of complement by therapeutic liposomes and other lipid excipient-based therapeutic products: prediction and prevention, Adv. Drug Deliv. Rev. 63 (2011) 1020–1030, https://doi.org/10.1016/j.addr.2011.06.017.
[37] J. Szebeni, Complement activation-related pseudoallergy: a stress reaction in blood triggered by nanomedicines and biologicals, Mol. Immunol. 61 (2014) 163–173, https://doi.org/10.1016/j.molimm.2014.06.038.
[38] A.S. Abu Lila, H. Kiwada, T. Ishida, The accelerated blood clearance (ABC) phenomenon: clinical challenge and approaches to manage, J. Control. Release 172 (2013) 38–47, https://doi.org/10.1016/j.jconrel.2013.07.026.
[39] T. Ishida, X. Wang, T. Shimizu, K. Nawata, H. Kiwada, PEGylated liposomes elicit an anti-PEG IgM response in a T cell-independent manner, J. Control. Release 122 (2007) 349–355, https://doi.org/10.1016/j.jconrel.2007.05.015.
[40] E.T. Dams, P. Laverman, W.J. Oyen, G. Storm, G.L. Scherphof, J.W. van Der Meer, F.H. Corstens, O.C. Boerman, Accelerated blood clearance and altered biodistribution of repeated injections of sterically stabilized liposomes, J. Pharmacol. Exp. Ther. 292 (2000) 1071–1079.
[41] M. Picard, J.P. Drolet, M.S. Masse, C.A. Filion, A.L. F, M. Fein, A. Copaescu, G.A. C. Isabwe, M. Blaquiere, M.N. Primeau, Safety of COVID-19 vaccination in patients with polyethylene glycol allergy: a case series, J Allergy Clin Immunol Pract 10 (2022) 620–625, e621, https://doi.org/10.1016/j.jaip.2021.11.021.
[42] L. Sercombe, T. Veerati, F. Moheimani, S.Y. Wu, A.K. Sood, S. Hua, Advances and challenges of liposome assisted drug delivery, Front. Pharmacol. 6 (2015) 286, https://doi.org/10.3389/fphar.2015.00286.
[43] D.C. Litzinger, A.M.J. Buiting, N. Vanrooijen, L. Huang, Effect of liposome size on the circulation time and Intraorgan distribution of amphipathic poly(ethylene glycol)-containing liposomes, Bba-Biomembranes 1190 (1994) 99–107, https://doi.org/10.1016/0005-2736(94)90038-8.
[44] O.G. de Jong, S.A.A. Kooijmans, D.E. Murphy, L.L. Jiang, M.J.W. Evers, J.P. G. Sluijter, P. Vader, R.M. Schiffelers, Drug delivery with extracellular vesicles: from imagination to innovation, Acc. Chem. Res. 52 (2019) 1761–1770, https://doi.org/10.1021/acs.accounts.9b00109.
[45] G. Storm, M.T. ten Kate, P.K. Working, I.A.J.M. Bakker-Woudenberg, Doxorubicin entrapped in sterically stabilized liposomes: effects on bacterial blood clearance capacity of the mononuclear phagocyte system, Clin. Cancer Res. 4 (1998) 111–115.
[46] A.P. Castano, P. Mroz, M.R. Hamblin, Photodynamic therapy and anti-tumour immunity, Nat. Rev. Cancer 6 (2006) 535–545, https://doi.org/10.1038/nrc1894.
[47] A.D. Bangham, M.M. Standish, J.C. Watkins, Diffusion of univalent ions across the lamellae of swollen phospholipids, J. Mol. Biol. 13 (1965) 238–252, https://doi.org/10.1016/s0022-2836(65)80093-6.
[48] D. Deamer, A.D. Bangham, Large volume liposomes by an ether vaporization method, Biochim. Biophys. Acta 443 (1976) 629–634, https://doi.org/10.1016/0005-2736(76)90483-1.
[49] F. Szoka Jr., D. Papahadjopoulos, Procedure for preparation of liposomes with large internal aqueous space and high capture by reverse-phase evaporation, Proc. Natl. Acad. Sci. USA 75 (1978) 4194–4198, https://doi.org/10.1073/pnas.75.9.4194.
[50] A. Jahn, W.N. Vreeland, D.L. DeVoe, L.E. Locascio, M. Gaitan, Microfluidic directed formation of liposomes of controlled size, Langmuir 23 (2007) 6289–6293, https://doi.org/10.1021/la070051a.
[51] A.G. Kohli, P.H. Kierstead, V.J. Venditto, C.L. Walsh, F.C. Szoka, Designer lipids for drug delivery: from heads to tails, J. Control. Release 190 (2014) 274–287, https://doi.org/10.1016/j.jconrel.2014.04.047.
[52] S. Du, Y. Guan, A. Xie, Z. Yan, S. Gao, W. Li, L. Rao, X. Chen, T. Chen, Extracellular vesicles: a rising star for therapeutics and drug delivery, J. Nanobiotechnol. 21 (2023) 231, https://doi.org/10.1186/s12951-023-01973-5.
[53] L. Tong, S. Zhang, R. Huang, H. Yi, J.W. Wang, Extracellular vesicles as a novel photosensitive drug delivery system for enhanced photodynamic therapy, Front. Bioeng. Biotechnol. 10 (2022) 1032318, https://doi.org/10.3389/fbioe.2022.1032318.
[54] J.M. Pitt, G. Kroemer, L. Zitvogel, Extracellular vesicles: masters of intercellular communication and potential clinical interventions, J. Clin. Invest. 126 (2016) 1139–1143, https://doi.org/10.1172/JCI87316.
[55] P. Lara, Huis In, R.V. 'tVeld, C. Jorquera-Cordero, A.B. Chan, F. Ossendorp, L. J. Cruz, Zinc-phthalocyanine-loaded extracellular vesicles increase efficacy and selectivity of photodynamic therapy in co-culture and preclinical models of colon cancer, Pharmaceutics 13 (2021), https://doi.org/10.3390/pharmaceutics13101547.
[56] Huis In, R.V. 'tVeld, P. Lara, M.J. Jager, R.I. Koning, F. Ossendorp, L.J. Cruz, M1-derived extracellular vesicles enhance photodynamic therapy and promote immunological memory in preclinical models of colon cancer, J. Nanobiotechnol. 20 (2022) 252, https://doi.org/10.1186/s12951-022-01448-z.
[57] S. Pan, L. Pei, A. Zhang, Y. Zhang, C. Zhang, M. Huang, Z. Huang, B. Liu, L. Wang, L. Ma, et al., Passion fruit-like exosome-PMA/Au-BSA@Ce6 nanovehicles for real-time fluorescence imaging and enhanced targeted photodynamic therapy with deep penetration and superior retention behavior in tumor, Biomaterials 230 (2020) 119606, https://doi.org/10.1016/j.biomaterials.2019.119606.
[58] Y. Jang, H. Kim, S. Yoon, H. Lee, J. Hwang, J. Jung, J.H. Chang, J. Choi, H. Kim, Exosome-based photoacoustic imaging guided photodynamic and immunotherapy for the treatment of pancreatic cancer, J. Control. Release 330 (2021) 293–304, https://doi.org/10.1016/j.jconrel.2020.12.039.
[59] M. Zhang, W. Shao, T. Yang, H. Liu, S. Guo, D. Zhao, Y. Weng, X.J. Liang, Y. Huang, Conscription of immune cells by light-activatable silencing NK-derived exosome (LASNEO) for synergetic tumor eradication, Adv. Sci. (Weinh) 9 (2022) e2201135, https://doi.org/10.1002/advs.202201135.
[60] C. Gong, X. Zhang, M. Shi, F. Li, S. Wang, Y. Wang, Y. Wang, W. Wei, G. Ma, Tumor exosomes reprogrammed by low pH are efficient targeting vehicles for smart drug delivery and personalized therapy against their homologous tumor, Adv. Sci. (Weinh) 8 (2021) 2002787, https://doi.org/10.1002/advs.202002787.
[61] H. Cheng, J.H. Fan, L.P. Zhao, G.L. Fan, R.R. Zheng, X.Z. Qiu, X.Y. Yu, S.Y. Li, X. Z. Zhang, Chimeric peptide engineered exosomes for dual-stage light guided plasma membrane and nucleus targeted photodynamic therapy, Biomaterials 211 (2019) 14–24, https://doi.org/10.1016/j.biomaterials.2019.05.004.
[62] D. Zhu, Y. Duo, M. Suo, Y. Zhao, L. Xia, Z. Zheng, Y. Li, B.Z. Tang, Tumor-exocytosed exosome/aggregation-induced emission luminogen hybrid nanovesicles facilitate efficient tumor penetration and photodynamic therapy, Angew. Chem. Int. Ed. Eng. 59 (2020) 13836–13843, https://doi.org/10.1002/anie.202003672.
[63] J. Du, Z. Wan, C. Wang, F. Lu, M. Wei, D. Wang, Q. Hao, Designer exosomes for targeted and efficient ferroptosis induction in cancer via chemo-photodynamic therapy, Theranostics 11 (2021) 8185–8196, https://doi.org/10.7150/thno.59121.
[64] H. Li, S. Li, Y. Lin, S. Chen, L. Yang, X. Huang, H. Wang, X. Yu, L. Zhang, Artificial exosomes mediated spatiotemporal-resolved and targeted delivery of epigenetic inhibitors, J. Nanobiotechnol. 19 (2021) 364, https://doi.org/10.1186/s12951-021-01107-9.
[65] H. Cao, H. Gao, L. Wang, Y. Cheng, X. Wu, X. Shen, H. Wang, Z. Wang, P. Zhan, J. Liu, et al., Biosynthetic dendritic cell-exocytosed aggregation-induced emission nanoparticles for synergistic photodynamic immunotherapy, ACS Nano 16 (2022) 13992–14006, https://doi.org/10.1021/acsnano.2c03597.
[66] C. Thery, S. Amigorena, G. Raposo, A. Clayton, Isolation and characterization of exosomes from cell culture supernatants and biological fluids, Curr. Protoc. Cell Biol. 3 (2006) 22, https://doi.org/10.1002/0471143030.cb0322s30. Chapter 3, Unit.
[67] M.S.S. Malys, C. Aigner, S.M.M. Schulz, H. Schachner, A.J.J. Rees, R. Kain, Isolation of Small extracellular vesicles from human sera, Int. J. Mol. Sci. 22 (2021), https://doi.org/10.3390/ijms22094653.
[68] Y.T. Tang, Y.Y. Huang, L. Zheng, S.H. Qin, X.P. Xu, T.X. An, Y. Xu, Y.S. Wu, X. M. Hu, B.H. Ping, et al., Comparison of isolation methods of exosomes and exosomal RNA from cell culture medium and serum, Int. J. Mol. Med. 40 (2017) 834–844, https://doi.org/10.3892/ijmm.2017.3080.
[69] M.A. Aziz, B. Seo, H.M. Hussaini, M. Hibma, A.M. Rich, Comparing two methods for the isolation of exosomes, J. Nucleic Acids 2022 (2022) 8648373, https://doi.org/10.1155/2022/8648373.
[70] P. Lara, S. Palma-Florez, E. Salas-Huenuleo, I. Polakovicova, S. Guerrero, L. Lobos-Gonzalez, A. Campos, L. Munoz, C. Jorquera-Cordero, M. Varas-Godoy, et al., Gold nanoparticle based double-labeling of melanoma extracellular vesicles to determine the specificity of uptake by cells and preferential accumulation in small metastatic lung tumors, J. Nanobiotechnol. 18 (2020) 20, https://doi.org/10.1186/s12951-020-0573-0.
[71] W. Zhang, C. Gong, Z. Chen, M. Li, Y. Li, J. Gao, Tumor microenvironment-activated cancer cell membrane-liposome hybrid nanoparticle-mediated synergistic metabolic therapy and chemotherapy for non-small cell lung cancer, J. Nanobiotechnol. 19 (2021) 339, https://doi.org/10.1186/s12951-021-01085-y.

[72] J. Wan, J. Wang, M. Zhou, Z. Rao, X. Ling, A cell membrane vehicle co-delivering sorafenib and doxorubicin remodel the tumor microenvironment and enhance immunotherapy by inducing immunogenic cell death in lung cancer cells, J. Mater. Chem. B 8 (2020) 7755–7765, https://doi.org/10.1039/d0tb01052a.
[73] S. Yun, S. Kim, K. Kim, Cellular membrane components-mediated Cancer immunotherapeutic platforms, Macromol. Biosci. 23 (2023) e2300159, https://doi.org/10.1002/mabi.202300159.
[74] V.D. Awasthi, D. Garcia, B.A. Goins, W.T. Phillips, Circulation and biodistribution profiles of long-circulating PEG-liposomes of various sizes in rabbits, Int. J. Pharm. 253 (2003) 121–132, https://doi.org/10.1016/s0378-5173(02)00703-2.
[75] H. Kang, Q. Wu, A. Sun, X. Liu, Y. Fan, X. Deng, Cancer cell Glycocalyx and its significance in Cancer progression, Int. J. Mol. Sci. 19 (2018), https://doi.org/10.3390/ijms19092484.
[76] J. Chin-Hun Kuo, J.G. Gandhi, R.N. Zia, M.J. Paszek, Physical biology of the cancer cell glycocalyx, Nat. Phys. 14 (2018) 658–669, https://doi.org/10.1038/s41567-018-0186-9.
[77] R.F. van Golen, T.M. van Gulik, M. Heger, Mechanistic overview of reactive species-induced degradation of the endothelial glycocalyx during hepatic ischemia/reperfusion injury, Free Radic. Biol. Med. 52 (2012) 1382–1402, https://doi.org/10.1016/j.freeradbiomed.2012.01.013.
[78] M.C. Woodle, M.S. Newman, J.A. Cohen, Sterically stabilized liposomes: physical and biological properties, J. Drug Target. 2 (1994) 397–403, https://doi.org/10.3109/10611869408996815.
[79] Y. Barenholz, Doxil(R)–the first FDA-approved nano-drug: lessons learned, J. Control. Release 160 (2012) 117–134, https://doi.org/10.1016/j.jconrel.2012.03.020.
[80] M. Danaei, M. Dehghankhold, S. Ataei, F. Hasanzadeh Davarani, R. Javanmard, A. Dokhani, S. Khorasani, M.R. Mozafari, Impact of particle size and polydispersity index on the clinical applications of lipidic nanocarrier systems, Pharmaceutics 10 (2018), https://doi.org/10.3390/pharmaceutics10020057.
[81] S. Behzadi, V. Serpooshan, W. Tao, M.A. Hamaly, M.Y. Alkawareek, E.C. Dreaden, D. Brown, A.M. Alkilany, O.C. Farokhzad, M. Mahmoudi, Cellular uptake of nanoparticles: journey inside the cell, Chem. Soc. Rev. 46 (2017) 4218–4244, https://doi.org/10.1039/c6cs00636a.
[82] R.R. Arvizo, O.R. Miranda, M.A. Thompson, C.M. Pabelick, R. Bhattacharya, J. D. Robertson, V.M. Rotello, Y.S. Prakash, P. Mukherjee, Effect of nanoparticle surface charge at the plasma membrane and beyond, Nano Lett. 10 (2010) 2543–2548, https://doi.org/10.1021/nl101140t.
[83] E. Papini, R. Tavano, F. Mancin, Opsonins and dysopsonins of nanoparticles: facts, concepts, and methodological guidelines, Front. Immunol. 11 (2020) 567365, https://doi.org/10.3389/fimmu.2020.567365.
[84] U. Isele, P. van Hoogevest, R. Hilfiker, H.G. Capraro, K. Schieweck, H. Leuenberger, Large-scale production of liposomes containing monomeric zinc phthalocyanine by controlled dilution of organic solvents, J. Pharm. Sci. 83 (1994) 1608–1616, https://doi.org/10.1002/jps.2600831117.
[85] L.R. de Haan, M.J. Reiniers, L.F. Reeskamp, A. Belkouz, L. Ao, S. Cheng, B. Ding, R.F. van Golen, M. Heger, Experimental conditions that influence the utility of 2′7′-dichlorodihydrofluorescein diacetate (DCFH(2)-DA) as a fluorogenic biosensor for mitochondrial redox status, Antioxidants (Basel) 11 (2022), https://doi.org/10.3390/antiox11081424.
[86] J.M. Bland, D.G. Altman, Statistical methods for assessing agreement between two methods of clinical measurement, Lancet 1 (1986) 307–310.
[87] S.M. Nunes, F.S. Sguilla, A.C. Tedesco, Photophysical studies of zinc phthalocyanine and chloroaluminum phthalocyanine incorporated into liposomes in the presence of additives, Braz. J. Med. Biol. Res. 37 (2004) 273–284, https://doi.org/10.1590/s0100-879x2004000200016.
[88] U. Isele, K. Schieweck, R. Kessler, P. van Hoogevest, H.G. Capraro, Pharmacokinetics and body distribution of liposomal zinc phthalocyanine in tumor-bearing mice: influence of aggregation state, particle size, and composition, J. Pharm. Sci. 84 (1995) 166–173, https://doi.org/10.1002/jps.2600840209.
[89] H. Isago, Optical Spectra of Phthalocyanines and Related Compounds, 2015, https://doi.org/10.1007/978-4-431-55102-7.
[90] T. Reinot, J.M. Hayes, G.J. Small, M.C. Zerner, Q-band splitting and relaxation of aluminum phthalocyanine tetrasulfonate, Chem. Phys. Lett. 299 (1999) 410–416, https://doi.org/10.1016/S0009-2614(98)01346-3.
[91] K. Liu, Y. Wang, J. Yao, Y. Luo, Origin of the Q-band splitting in the absorption spectra of aluminum phthalocyanine chloride, Chem. Phys. Lett. 438 (2007) 36–40, https://doi.org/10.1016/j.cplett.2007.02.048.
[92] K. Nakai, J. Usami, N. Kobayashi, Metal phthalocyanine showing four-peak Q-band similar to metal-free phthalocyanines: nickel 1,4-di(trifluorosulfonyl)-phthalocyanine, J. Porphyrins Phthalocyanines 11 (2007) 222–227, https://doi.org/10.1142/s108842460700028x.
[93] M. Más-Montoya, R.A.J. Janssen, The effect of H- and J-aggregation on the Photophysical and photovoltaic properties of small thiophene–pyridine–DPP molecules for bulk-heterojunction solar cells, Adv. Funct. Mater. 27 (2017) 1605779, https://doi.org/10.1002/adfm.201605779.
[94] S. Moradi, A. Nowroozi, M. Shahlaei, Shedding light on the structural properties of lipid bilayers using molecular dynamics simulation: a review study, RSC Adv. 9 (2019) 4644–4658, https://doi.org/10.1039/C8RA08441F.
[95] M. Whalley, 182. Conjugated macrocycles. Part XXXII. Absorption spectra of tetrazaporphins and phthalocyanines. Formation of pyridine salts, J. Chem. Soc. (Resumed) (1961) 866–869, https://doi.org/10.1039/JR9610000866.
[96] B. Mesquita, A. Singh, C.P. Masdeu, N. Lokhorst, E.R. Hebels, M. van Steenbergen, E. Mastrobattista, M. Heger, C.F. van Nostrum, S. Oliveira, Nanobody-mediated targeting of zinc phthalocyanine with polymer micelles as nanocarriers, Int. J. Pharm. (2024) 124004, https://doi.org/10.1016/j.ijpharm.2024.124004.
[97] L.A. Mulcahy, R.C. Pink, D.R. Carter, Routes and mechanisms of extracellular vesicle uptake, J. Extracell Vesicles 3 (2014), https://doi.org/10.3402/jev.v3.24641.
[98] C. Castillo Ferrer, K. Berthenet, G. Ichim, Apoptosis - fueling the oncogenic fire, FEBS J. 288 (2021) 4445–4463, https://doi.org/10.1111/febs.15624.
[99] M. Mathieu, L. Martin-Jaular, G. Lavieu, C. Thery, Specificities of secretion and uptake of exosomes and other extracellular vesicles for cell-to-cell communication, Nat. Cell Biol. 21 (2019) 9–17, https://doi.org/10.1038/s41556-018-0250-9.
[100] V. Depraetere, "eat me" signals of apoptotic bodies, Nat. Cell Biol. 2 (2000) E104, https://doi.org/10.1038/35014098.
[101] T. Kang, Q. Zhu, D. Wei, J. Feng, J. Yao, T. Jiang, Q. Song, X. Wei, H. Chen, X. Gao, et al., Nanoparticles coated with neutrophil membranes can effectively treat Cancer metastasis, ACS Nano 11 (2017) 1397–1411, https://doi.org/10.1021/acsnano.6b06477.
[102] A. Pitchaimani, T.D.T. Nguyen, S. Aryal, Natural killer cell membrane infused biomimetic liposomes for targeted tumor therapy, Biomaterials 160 (2018) 124–137, https://doi.org/10.1016/j.biomaterials.2018.01.018.
[103] L. Zhang, R. Li, H. Chen, J. Wei, H. Qian, S. Su, J. Shao, L. Wang, X. Qian, B. Liu, Human cytotoxic T-lymphocyte membrane-camouflaged nanoparticles combined with low-dose irradiation: a new approach to enhance drug targeting in gastric cancer, Int. J. Nanomedicine 12 (2017) 2129–2142, https://doi.org/10.2147/IJN.S126016.
[104] H. Cao, Z. Dan, X. He, Z. Zhang, H. Yu, Q. Yin, Y. Li, Liposomes coated with isolated macrophage membrane can target lung metastasis of breast Cancer, ACS Nano 10 (2016) 7738–7748, https://doi.org/10.1021/acsnano.6b03148.
[105] N. Mehraban, P.R. Musich, H.S. Freeman, Synthesis and encapsulation of a new zinc phthalocyanine photosensitizer into polymeric nanoparticles to enhance cell uptake and phototoxicity, Appl. Sci. 9 (2019).
[106] M. Cozzolino, L. Pesce, D. Pezzuoli, C. Montali, L. Brancaleon, L. Cavanna, S. Abbruzzetti, A. Diaspro, P. Bianchini, C. Viappiani, Apomyoglobin is an efficient carrier for zinc phthalocyanine in photodynamic therapy of tumors, Biophys. Chem. 253 (2019) 106228, https://doi.org/10.1016/j.bpc.2019.106228.
[107] D. Zhao, Q. Chen, H. Song, S. Luo, P. Ge, Y. Wang, J. Ma, Z. Li, X. Gao, X. Zhao, et al., Theranostic micelles combined with multiple strategies to effectively overcome multidrug resistance, Nanomedicine 13 (2018) 1517–1533, https://doi.org/10.2217/nnm-2017-0393.
[108] H. Abrahamse, M.R. Hamblin, New photosensitizers for photodynamic therapy, Biochem. J. 473 (2016) 347–364, https://doi.org/10.1042/BJ20150942.
[109] A. Ayala, M.F. Munoz, S. Arguelles, Lipid peroxidation: production, metabolism, and signaling mechanisms of malondialdehyde and 4-hydroxy-2-nonenal, Oxidative Med. Cell. Longev. 2014 (2014) 360438, https://doi.org/10.1155/2014/360438.
[110] A.A. Nanji, S. Hiller-Sturmhofel, Apoptosis and necrosis: two types of cell death in alcoholic liver disease, Alcohol Health Res. World 21 (1997) 325–330.
[111] I.O.L. Bacellar, M.S. Baptista, Mechanisms of photosensitized lipid oxidation and membrane Permeabilization, ACS Omega 4 (2019) 21636–21646, https://doi.org/10.1021/acsomega.9b03244.
[112] J. Kim, O.A. Santos, J.H. Park, Selective photosensitizer delivery into plasma membrane for effective photodynamic therapy, J. Control. Release 191 (2014) 98–104, https://doi.org/10.1016/j.jconrel.2014.05.049.
[113] M. Heger, Editor's inaugural issue foreword: perspectives on translational and clinical research, J. Clin. Transl. Res. 1 (2015) 1–5.
[114] J.R. Alonzo, C. Venkataraman, M.S. Field, P.J. Stover, The mitochondrial inner membrane protein MPV17 prevents uracil accumulation in mitochondrial DNA, J. Biol. Chem. 293 (2018) 20285–20294, https://doi.org/10.1074/jbc.RA118.004788.
[115] M.E. de Araujo, L.A. Huber, Subcellular fractionation, Methods Mol. Biol. 357 (2007) 73–85, https://doi.org/10.1385/1-59745-214-9:73.
[116] M. Li, M.I. van Raath, S. Khakpour, A. Secilir, B.C. Sliggers, X. Huang, B. Ding, G. Storm, R.R. van der Hulst, A. de Kroon, et al., In vivo assessment of thermosensitive liposomes for the treatment of port wine stains by antifibrinolytic site-specific pharmaco-laser therapy, Pharmaceutics 12 (2020), https://doi.org/10.3390/pharmaceutics12060591.
[117] G. Rouser, S. Fkeischer, A. Yamamoto, Two dimensional then layer chromatographic separation of polar lipids and determination of phospholipids by phosphorus analysis of spots, Lipids 5 (1970) 494–496, https://doi.org/10.1007/BF02531316.
[118] P.E. Feuser, A.P. Cordeiro, G. de Bem Silveira, M.E.A. Borges Correa, P.C. Lock Silveira, C. Sayer, P.H.H. de Araujo, R.A. Machado-de-Avila, A.G. Dal Bo, Co-encapsulation of sodium diethyldithiocarbamate (DETC) and zinc phthalocyanine (ZnPc) in liposomes promotes increases phototoxic activity against (MDA-MB 231) human breast cancer cells, Colloids Surf. B: Biointerfaces 197 (2021) 111434, https://doi.org/10.1016/j.colsurfb.2020.111434.
[119] J. Ma, D. Chen, Y. Li, Y. Chen, Q. Liu, X. Zhou, K. Qian, Z. Li, H. Ruan, Z. Hou, et al., Zinc phthalocyanine-soybean phospholipid complex based drug carrier for switchable photoacoustic/fluorescence image, multiphase photothermal/photodynamic treatment and synergetic therapy, J. Control. Release 284 (2018) 1–14, https://doi.org/10.1016/j.jconrel.2018.06.005.
[120] Z. Chen, Y.Y. Zhao, L. Li, Z. Li, S. Fu, Y. Xu, B.Y. Zheng, M. Ke, X. Li, J.D. Huang, A sulfur-bridging sulfonate-modified zinc(II) phthalocyanine nanoliposome possessing hybrid type I and type II photoreactions with efficient photodynamic

anticancer effects, Molecules 28 (2023), https://doi.org/10.3390/molecules28052250.

[121] J. Ma, Y. Li, G. Liu, A. Li, Y. Chen, X. Zhou, D. Chen, Z. Hou, X. Zhu, Novel theranostic zinc phthalocyanine-phospholipid complex self-assembled nanoparticles for imaging-guided targeted photodynamic treatment with controllable ROS production and shape-assisted enhanced cellular uptake, Colloids Surf. B: Biointerfaces 162 (2018) 76–89, https://doi.org/10.1016/j.colsurfb.2017.10.061.

[122] P.E. Feuser, J.C. Possato, R. Scussel, R. Cercena, P.H.H.D. Araújo, R.A. Machado-de-Ávila, A.G.D. Bó, In vitro phototoxicity of zinc phthalocyanine (ZnPc) loaded in liposomes against human breast cancer cells, J. Porphyrins Phthalocyanines 25 (2021) 153–161, https://doi.org/10.1142/s1088424621500073.